Communications Biology

https://doi.org/10.1038/s42003-026-09653-4

Article in Press

Agent-based modeling of cellular dynamics in adoptive cell therapy

Received: 26 March 2025

Accepted: 27 January 2026

Cite this article as: Wang, Y., Casarin, S., Daher, M. *et al.* Agent-based modeling of cellular dynamics in adoptive cell therapy. *Commun Biol* (2026). https://doi.org/10.1038/s42003-026-09653-4

Yujia Wang, Stefano Casarin, May Daher, Vakul Mohanty, Merve Dede, Mayra Shanley, Eleonora Dondossola, Ludovica La Posta, Rafet Başar, Katayoun Rezvani & Ken Chen

Agent-based modeling of cellular dynamics in adoptive cell therapy

Yujia Wang[1], Stefano Casarin[2 3 4], May Daher[5], Vakul Mohanty[1], Merve Dede[1], Mayra Shanley[5], Eleonora Dondossola[6], Ludovica La Posta[6], Rafet Başar[5], Katayoun Rezvani[5], Ken Chen[1*]

[1] Department of Bioinformatics and Computational Biology, The University of Texas MD Anderson Cancer Center, Houston, TX, USA.

[2] Center for Precision Surgery, Houston Methodist Research Institute, Houston, TX, USA.

[3] Department of Surgery, Houston Methodist Hospital, Houston, TX, USA.

[4] LaSIE, UMR 7356 CNRS, La Rochelle Université, La Rochelle, France.

[5] Department of Stem Cell Transplantation and Cellular Therapy, The University of Texas MD Anderson Cancer Center, Houston, TX, USA

[6] Division of Cancer Medicine, Department of Genitourinary Medical Oncology, The University of Texas MD Anderson Cancer Center, Houston, TX, USA.

[*]Corresponding author: Ken Chen. Email: kchen3@mdanderson.org.

Abstract

Adoptive cell therapies (ACT) leverage tumor-immune interactions to cure cancer. Despite promising phase I/II clinical trials of chimeric-antigen-receptor natural killer (CAR-NK) cell therapies, molecular mechanisms and cellular properties required to achieve clinical benefits in broad cancer spectra remain underexplored. While *in vitro* and *in vivo* experiments are essential, they are expensive, laborious, and limited to targeted investigations. Here, we present ABMACT (Agent-Based Model for Adoptive Cell Therapy), an *in silico* approach employing agent-based models (ABM) to simulate the continuous course and dynamics of an evolving tumor-immune ecosystem, consisting of heterogeneous "virtual cells" created based on knowledge and omics data observed in experiments and patients. Applying ABMACT in multiple therapeutic contexts indicates that to achieve optimal ACT efficacy, it is key to enhance immune cellular proliferation, cytotoxicity, and serial killing capacity. With ABMACT, *in silico* trials can be performed systematically to inform ACT product development and predict optimal treatment strategies.

Introduction

Adoptive cell therapies (ACT) have shown substantial progress in combating cancer and other diseases[1–9]. By administrating lymphocytes with intrinsic or engineered antitumoral capabilities, ACTs harness the power of the immune system to eliminate tumors[9]. Recent Chimeric-antigen-receptor natural killer (CAR-NK) cell therapies have been identified as a promising alternative to CAR-T cell therapies, given their ability to address multiple limitations of CAR-T therapies[2,10–15]. As a low-cost, low-toxicity, off-the-shelf solution, various CAR-NK cell therapy products have burgeoned to deliver benefits in a broad spectrum of clinical applications[12,13]. CAR extracellular domain engineering provides specificity for anti-tumor effects, such as anti-CD123 targeting acute myeloid leukemia cells[16], anti-CD19 targeting B cell lymphoma[17], and anti-CD70 for hematological malignancies and solid tumors[18]. Various genetic engineering approaches can augment CAR-NK cell functions: armoring NK cells with co-stimulatory cytokine vectors such as IL-15[19], IL-21[20], and STING agonist[21] can boost NK cell proliferation and killing capability, while CRISPR editing such as *CISH* deletion[22] increases NK cell metabolic fitness. In the case of cord-blood derived CAR-NK cells, donor characteristics can dictate CAR-NK function and clinical efficacy. Increased inflammation, hypoxia, and cellular stress have been associated with suboptimal cord blood preservation, and CAR-NK cells engineered from these cords have reduced anti-tumor efficacy[5,23]. Despite significant advances,

applications of CAR-NK ACT are predominantly in preclinical and phase-I/II trial stages[1,14], highlighting both the potential and need for further investigation.

As "living drugs", ACTs present distinct opportunities and challenges in clinical development[24]. ACT achieves treatment responses through interactions between the product and the target cells. The cell products are often genetically modified to boost therapeutic potential. However, both aspects are difficult to assess. While *in vitro* and *in vivo* models have been instrumental in advancing ACT development, they are often costly, labor-intensive, and limited in their ability to replicate the complexity of the interactions between the human immune system and the tumor microenvironment (TME)[25,26]. The TME is characterized by diverse and evolving cell populations, along with a rich and dynamic molecular environment, which cannot be fully recapitulated using traditional cell-line models[26]. Organoids are engineered to replicate the morphology and functions of tissues and organs, yet [27]still struggle with repeatability, cell maturation, and accurately replicating the complexity of native tissue[27]. Although patient-derived xenograft (PDX) animal models aim to reflect TME heterogeneity, they still diverge significantly from human physiology and pharmacology, limiting their translational relevance[25]. Perturbing PDX models is time consuming and expensive, limiting exploration and hypothesis testing. Further, evaluating treatment responses, particularly cellular kinetics and molecular interactions, such as peak concentration and target interaction rates, remains a challenge in these experimental systems due to the difficulties of continuous monitoring[24]. A more comprehensive understanding of multi-scale dynamics at both cellular and sub-cellular level is essential to advance ACT development. This includes capturing the heterogeneous and evolving cell populations, modeling phenotypic and functional states of individual cells, and accounting for their molecular variations. Addressing these challenges requires innovative approaches that combine experimental data with mechanistic and computational modeling, which have the potential to provide deeper insights into complex biological dynamics.

Mathematical and computational models have been utilized to understand complex biological systems, spanning from organisms to molecules[28–33]. Recent advancements in ACTs and the growing availability of data have facilitated their modeling, though further efforts are needed, particularly in emerging areas such as engineered NK cell therapy. Machine learning models, such as random forests, support vector machines, and neural networks, estimate statistical relationships between features (e.g., cell counts, cell states, and experimental conditions) and outcomes, and those amongst features by optimizing predictive accuracy against data. However, the learned parameters are often difficult to interpret in terms of underlying biological mechanisms. This limitation reduces their utility for generating mechanistic insights and translating findings into clinical applications[34]. Sparse data points collected in *in vitro* or *in vivo* experiments also restrict these models' ability to accurately capture the dynamics of ACT. Mechanistic models such as ordinary differential equations (ODE), partial differential equations (PDE), and stochastic differential equations (SDE) have been developed to describe the kinetics of cell populations and cytokines in the TME[35]. These approaches offer improved efficiency and mathematical interpretability and are more suited in modeling low-dimensional cell properties and spatial gradients than single-cell level specifications[36]. Among the vast suite of *in silico* models, Agent-Based Models (ABM)[37,38], also known as individual-based models, offer the unique advantage of simulating the tumor microenvironment using a bottom-up approach to model individual cell behaviors[28,39]. ABMs represent cells and molecules in the TME as agents and environment attributes, in which the behaviors of each type of agent are coded via simplifications and approximations of biological processes[37,38]. This enables ABM to have high temporal, spatial, and multi-scale data granularity and interpretability, overcoming challenges in above mentioned modeling methods such as ODE and neural networks[28]. Extensive research has demonstrated the potential of using ABM to

reproduce the complex interactions in the TME and predict tumor progression or treatment outcomes[36,40–43]. Several studies have attempted to model heterogeneity of cell states by summarizing functional effects of genes[36,39,41,44]. However, these effects are usually binarized as positive and negative regulators of cellular functions without considering their relative importance. Moreover, the application of ABMs to cellular immunotherapies, particularly engineered NK cell therapies, remain unexplored. Several critical questions must be addressed: How can a system of cell agents be designed to sufficiently capture the diversity of cell types and phenotypic transitions in NK-ACT? How can molecular profiles be integrated with cellular functions to model functional heterogeneity? How can knowledge and data be balanced to ensure both biological interpretability and predictive accuracy?

To investigate these questions, we have developed ABMACT, a mechanistic modeling framework that reconstructs cellular dynamics of an evolving tumor-immune ecosystem, consisting of "virtual" immune cells and tumor cells defined by immunological knowledge and single cell molecular profiles obtained in experiments. We focused on NK cells in this first study and constructed an ABM with submodules of cellular functions and cell-cell interactions based on our biological knowledge of NK cells and experimental data.

Results

A cell-level mechanistic modeling framework for NK-ACT

ABMACT is a computer simulation framework for studying cell population dynamics and interactions in ACT using ABM (**Figure 1**). Cell agents, the building blocks of the ABMs, are determined based on domain knowledge of interacting cell populations (**Figure 1 Step1**)[2,12,13,15,45]. NK cells are *ex vivo* expanded to express activating receptors such as *CD16, NKG2D*, and activating Killer cell immunoglobulin-like receptors (KIRs) and are "licensed" to kill[12,45]. Cytotoxic killing is the primary mechanism determining therapeutic responses in ACT[15], placing cytotoxic NK cells (N_c) and tumor cells (B, such as B cell lymphoma) interactions in the center of modeling. However, activation and repeated killing can induce exhaustion, resulting in NK dysfunction and cancer immune evasion [46]. While NK cells were believed to act short-term as part of innate immunity, multiple recent studies have highlighted their capacity to develop a "vigilant" phenotype – long living, dormant, and reactive to second pathogen stimulation[47–49]. To model the fate transitions of N_c, we include exhausted NK cell agents (N_E) and vigilant NK cell agents (N_V). Cellular processes such as proliferation, exhaustion, death, antigen recognition, and migration have previously been modeled using quantitative frameworks[24,41,50,51]. Building on these studies, we implemented biologically grounded mathematical rules and parameterizations to govern cell agent behaviors in our model (**Methods – Cell agent design**). Specifically, NK cell proliferation was modeled as cytokine-dependent, influenced by tumor presence and natural decay of proliferation rate. Exhaustion was represented by a linear decline in its serial killing capacity (SKC, s) such that NK cells transition from cytotoxic (N_C) to exhausted (N_E) states when the cumulated number of tumor cells killed ($\sum \mathrm{I_{kill}}$) equals to its initial capacity ($\mathrm{S_0}$). Non-exhausted cytotoxic NK cells can instead transform into the vigilant (N_V) phenotype upon tumor clearance. Details are provided in **Supplementary Materials 1**.

The increasing availability of single-cell molecular profiling data provides an unprecedented opportunity to model functional heterogeneity at cellular resolution. To achieve so, we quantified the effects of genes and pathways on cellular functions such as cytotoxicity. In this study, we used paired single-cell RNA-seq (scRNA-seq) and phenotype data from the xenograft lymphoma mouse models in Li et al.[23] to select and

estimate a subset of genetic features using linear mixed effect regression. [52]Gene expression profiles are randomly assigned to the cell agents and translated to functional properties through the estimated effects. As a result, cell agents unbiasedly represent rich molecular profiles, modeling variations in individual cellular fates and collective populational dynamics (**Figure 1 Step 2, Methods -** Integrate functional genetic effects in cell agents).

Model calibrations were performed on functional data obtained from *in vitro* autonomous growth in Liu et al.[19], rechallenge assays in Marin et al.[5] and Shanley et al. [20]. Joint calibration and evaluation were performed on the lymphoma mice model in Li et al. [23] and glioblastoma mice model in Shanley et al.[20] Independent evaluation of calibrated cell agents were performed on a blood cancer tumor-NK cell co-culture dataset in Dufva et al.[52] (**Figure 1 Step 3, Methods - Simulation**). By obtaining *in silico* replica of the *in vivo* systems, we can further perturb the models to augment experimental observations, discover key drivers to effective tumor control, and explore biological and therapeutic conditions (**Figure 1 Step 4, Methods - Feature importance sensitivity analysis**).

Figure 1: A mechanistic cell-level in silico modeling framework to elucidate cellular characteristics and cell population dynamics.

[Figure 1]

a) Workflow diagram of Agent-Based Modeling for Adoptive Cell Therapy (ABMACT). Step 1: Cell agent design. Four cell types are included in ABMACT: cytotoxic NK cells, exhausted NK cells, Vigilant NK cells, and tumor cells. Step 2: Embed cell-level genetic effects. Functional effects of significant genes and pathways regulating NK cell cytotoxicity are derived from paired longitudinal scRNA-seq data and mice model experiment [23] (Methods 4.2). The coefficients, multiplied with randomly sample expression profiles in individual cytotoxic cell agents, contribute to variations in cytotoxic killing capability. Step 3: Cell agents interact in 2D simulated TME to model tumor-immune interactions over time. ABMs are calibrated on *in vitro* and *in vivo* data. Step 4: Applications of calibrated ABMACT cell agent models in augmenting experimental observations and predicting future trends, tumor control driver discovery through aggregated simulations, and in-silico treatment simulations. Figure created with Biorender.

ABMACT recapitulates differential tumor control in mouse models

We examined whether ABMACT can reproduce the *in vivo* dynamics of NK cell therapy in mouse models and account for the differential tumor control across treatment conditions. To this end, cell agents were parametrized at the level of functional properties to capture differences across phenotypes. Recognizing that heterogeneity also exists within the same cell type or state, we further parametrize NK cell cytotoxicity from functional genetic effects. The identified NK cell cytotoxicity genes and GO Biological Process (GOBP) pathways included both canonical markers and previously under-characterized candidates (**Figure 2a, Supplementary Materials 2)**. *CD226*[53] and *PDCD1*[54] encode well-established activating and inhibitory receptor, respectively. Notably, *NFKBIA* was negatively associated with tumor load, despite its conventional classification as a stress-response gene. Consistent with our finding, Tang et al.[55] reported enrichment of *NKFBIA* in a cytotoxic $CD56^{dim}CD16^{hi}$ NK subset characterized by inflammatory and immune-recruiting signatures, suggesting a context-dependent role of *NKFBIA* in NK cell cytotoxicity. The derived coefficients and randomly sampled scRNA expression values were used to initialize cytotoxic NK cell agents, thereby mimicking the heterogenous NK cell population at the onset of treatment.

Lymphoma Mouse Model

We first investigated the therapeutic effects of engineered CAR-NK cells on a CD19+ lymphoblastoid cell line in immunodeficient mice in Li et al.[56]. Best fitted parameter sets were found by iterative grid search and minimizing a total loss function L_{total} that balance sensitivity to local fluctuations, robustness to noise, and fidelity to global tumor control dynamics (**Methods – Evaluation metrics**). ABMACT achieved good fitting to the tumor volume data measured by bioluminescence imaging for all the three NK cell products: non-transduced NK (NT-NK), CD19 CAR-NK and CD19IL15 CAR-NK. Particularly, the CD19IL15

CAR-NK product showed more effective tumor control as compared to NT-NK and CD19 CAR-NK cells, with tumor clearance by day 14 post-engraftment (**Figure 2b**), recapitulating the *in vivo* experiments. With ABMACT's ability to simulate continuous time courses, the differential tumor-killing capacity of the three NK cell products were depicted as continuous time trajectories, beyond the original time snaps (**Figure 2c**). ABMACT further delineated the cause of tumor cell death as NK cytotoxicity mediated death (**Figure 2d**) and programmed death (**Figure 2e**).

The CD19IL15 CAR-NK cell population expanded faster than the other two groups (**Figure 2f**), showing negative correlation with the tumor burden (Pearson's $R = -0.35$, $p<0.005$). Cytotoxic NK cells, which constituted a large proportion of the total population throughout the 15-day simulation, had the fastest expansion in the CD19IL15CAR-NK cell group, contrasting with rapid decline in the CD19 CAR-NK cell and NT-NK cell groups (**Figure 2g**). The CD19IL15 CAR-NK cells also showed lower degree of exhaustion as compared with the other two groups (**Figure 2h**). However, lower exhaustion levels do not always coincide with more efficacious tumor control. Although CD19 CAR-NK cells appeared less exhausted than the NT-NK cells, tumors treated with the CD19 CAR-NK cells outgrew those treated with the NT-NK cells (**Figure 2c**). In the CD19IL15CAR-NK cell group, the vigilant phenotype emerged as tumor cells were cleared, indicating successful transition of surviving cytotoxic NK cells in the TME (**Figure 2i**).

We further attributed the NK cell dynamics to individual cellular properties. Based on parameters from the best-fitting results, we found that CD19IL15 CAR-NK cells had superior viability and killing capacity as compared to other two groups (**Figure 2j**). In addition to enhanced proliferation and lower death rates, higher cytotoxicity p_{kill} at the beginning of treatment, and higher serial killing capacity (SKC) S_0, measured by the number of tumor cells one NK cell could kill before exhaustion, enabled CDIL15 CAR-NK cells to exert repeated tumor lysis at a high success rate. The systematic effects of the cellular properties resulted in stronger interactions between tumor cells and cytotoxic NK cells, measured by the proportions of tumor cells collocated with cytotoxic NK cells, in the CD19IL15 CAR-NK cell treatment group than the other two treatment groups (**Figure 2k**).

By deconvoluting the empirical cell dynamics to quantitative properties, we identified potential mechanisms underlying the differential tumor control observed by Li et al.[23] In the original experiment, lower tumor growth was observed in the NT-NK group compared to CD19 CAR-NK group (**Figure S3b**), diverging from the expectation that NT-NKs would perform worse than CAR-engineered NK cells. The seemingly counterintuitive results motivated us to investigate the underlying functional properties and mechanisms using estimated cell agent properties. While equipped with CAR, CD19 CAR-NK cells were characterized with a higher death rate (d_C) and lower serial killing (S_0) compared to NT-NK cells, suggesting reduced survival and increased susceptibility to exhaustion. The pattern is consistent with activation induced exhaustion[46], where CD19CAR NK cells undergo strong activation upon CD19 engagement but lack IL-15-mediated persistence. Supporting this interpretation, metabolic profiling of CD19CAR NK cells post-infusion revealed reduced oxidative phosphorylation and glycolysis relative to NT NK cells (**Figure S8b**), consistent with impaired tumor control ability.

In lymphoma model, the optimal fitting results were found at an effector-to-target ratio (ETR) of 1:1, which was much lower than the set-up condition in the in vivo mice models (50:1). We speculated that the differences could be due to the reduction of ETR at tumor sites from the ETR at infusion. The challenge of NK cell infiltration or homing to tumor sites have been previously reported and a limiting factor to NK-ACT efficacy[57,58]. In the study by Li et al., NK cells were infused through mouse tail veins and therefore it

is likely that only a fraction of NK cells infiltrated tumor sites. We assumed the initial infiltration NK cell population comprising entirely of cytotoxic NK cells to reduce modeling complexity, while NK cell activation, exhaustion, and ineffective transduction could reduce the actual number of cytotoxic NK cells homed to tumor sites and inflate the estimated ETR.

Incorporating genetic effects enabled the model to capture intercellular heterogeneity in cytotoxic killing probabilities. Integrating scRNA-seq data by setting the genetic effect parameter $b > 0$ improved the overall modeling accuracy as reflected by a reduction in total loss L_{total} (p-val=0.034, **Figure 2l, Supplementary Materials 3.3**). Models without genetic effects assumed a constant population-average killing rate, thereby neglecting variability in cytotoxicity among NK cells (**Figure S4f-g**). Fine-tuning the precise magnitude of yields marginal changes in fit, suggesting that enabling heterogeneity through a positive genetic effect parameter b is more critical than optimizing its exact scale.

Figure 2 Modeling NK-tumor cell interactions in lymphoma mice models using ABMACT framework.

[Figure 2]

(a) Genes and pathways modulating NK cell cytotoxicity identified using LME models of tumor loads in Li et al.[23]. Confidence interval: 95%. P-value adjusted by Benjamini-Hochberg correction for multiple-testing. (b) ABMACT simulations recapitulated normalized tumor dynamics in lymphoma mouse models. Comparison of simulated data with observed data using normalized tumor progression ratios between experimental groups and the tumor-only control group. (c) Tumor progression calculated by fold changes with respect to the initial tumor population at the start of the simulation. (d) The cumulative proportion of tumor cell death due to cytotoxic killing by NK cells. (e) The cumulative proportion of tumor cell death due to programmed death. (f) Total NK cell population fold changes with respect to the initial NK cell population. Normalized by NK cell count at day 0 of simulation when NK cells were added. Simulated ratios of (g) cytotoxic NK cells, (h) exhausted NK cells, and (i) vigilant NK cells with respect to the total NK cell population in the lymphoma model. (j) Best-fit cytotoxic NK cell proliferation rate at baseline (t0 of simulation), death rate, cytotoxicity (probability of killing a tumor cell upon contact) at baseline, and serial killing capacity that minimized the total loss for three treatment groups. (k) Interaction rate between tumor cells and cytotoxic NK cells in the lymphoma mouse model. Interaction rate calculated by the ratio between tumor cells co-locating with cytotoxic NK cells and the total tumor cell count. (l) Total loss (L_{total}) with genetic effects ($b > 0$) and without ($b = 0$) in modeling the lymphoma mouse model. Results aggregated from the top ten fittings based on MSE. Interval bands of 2 s.e. were calculated using a bootstrap of 1000 iterations.

Glioblastoma Mouse Model

To explore the potential of ABMACT in studying a broad spectrum of cancers, we further evaluated it in a glioblastoma (GBM) mouse model, which examines the therapeutic benefits of *ex vivo* expanded NK cells in kill GBM cell lines in immunodeficient mice (**Figure 3a**). The growth rate of GSC20 GBM tumor cells were estimated to be lower than Raji lymphoma (0.223 per day vs 0.445 per day), requiring a lower ETR (1:5 vs 3:1). Similar to the CD19IL15 CAR-NK cells in lymphoma model, cytokine-armed NK cells (IL-21 and IL-15 NK cells) showed more significant tumor control than NT-NK cells (**Figure 3b**). Tumor clearances were achieved in both IL-21 and IL-15 NK cells, with the highest proportions of cancer cell deaths induced by IL-21 NK cell cytotoxicity (**Figure 3c**). In the NT-NK cell group, tumor cells had sustained growth, with minimal reductions that were largely contributed by programmed deaths (**Figure 3d**). Despite having higher death rates than the IL-15 NK cells, the higher proliferation p_c, cytotoxicity p_{kill}, and SKC S_0 of the IL-21 NK cells contributed to more rapid tumor control (**Figure 3e**). NK cells with cytokine-expressing vectors showed faster initial NK cell population expansion than the NT-NK cells (**Figure 3f**). However, the early cytotoxicity towards tumor cells in the IL-15 NK cell group also resulted in early drops in cytotoxic population (**Figure 3g**) and exhaustion (**Figure 3h**). The time of population shrinkage concorded with tumor clearance, which aligned with prior studies of NK cell dynamics[48,59,60]. Similar to CD19IL15 CAR-NK cells in lymphoma mouse model, a small proportion of vigilant NK cells emerged upon tumor clearance (**Figure 3i**).

Independent Validation

To assess the generalizability of ABMACT in new NK-ACT studies, we used the calibrated non-transduced NK (NT-NK) cell agents to reproduce co-culture experiments with K562 myeloid leukemia cell line reported by Dufva et al[52] (**Methods – Independent validation**). Simulated NK-tumor cell co-culture reproduced tumor reduction at 24 hours ($43.05 \pm 2.62\%$ simulated vs 41.51% observed, p-val=0.59, **Figure 3j**). In addition, we found a similar percentage of effector NK cells subsets, denoted as cytotoxic NK cell in ABMACT and activated NK cell by Dufva et al., at the end of the 24-hour co-culture ($88.59 \pm 1.53\%$ simulated vs 87.67% observed, p-val=0.57) (**Figure 3k**). This exercise demonstrates ABMACT can be reasonably applied on independent datasets deriving from similar cell-lines without re-calibration, supporting its robustness and generalizability across experimental platforms.

Figure 3 Modeling NK-tumor cell interactions in glioblastoma (GBM) mice models and independent validation using ABMACT framework.

[Figure 3]

(a) ABMACT simulations recapitulated normalized tumor dynamics in GBM mouse models. Comparison of simulated data with observed data using normalized tumor progression ratios between experimental groups and the tumor-only control group. (b) Tumor progression calculated by fold changes with respect to the initial tumor population at the start of the simulation. (c) The cumulative proportion of tumor cell death due to cytotoxic killing by NK cells. (d) The cumulative proportion of tumor cell death due to programmed death. (e) Best-fit cytotoxic NK cell proliferation rate at baseline (t0 of simulation), death rate, cytotoxicity (probability of killing a tumor cell upon contact) at baseline, and serial killing capacity that minimized the total loss for three treatment groups. (f) Total NK cell population fold changes with respect to the initial NK cell population. Normalized by NK cell count at day 7 of simulation when NK cells were added. Simulated ratios of (g) cytotoxic NK cells, (h) exhausted NK cells, and (i) vigilant NK cells with respect to the total NK cell population in the lymphoma model. (j-k) Independent study validation on Dufva et al.[52] (j) Percentage of tumor reduction at 24-hour in the K562 cell line co-culture experiment and (k) percentage of cytotoxic (activated) NK cells among the total NK cell population using NT-NK cell agents calibrated on Li et al.[23] lymphoma mouse model. Simulations were repeated 10 times. Comparison of tumor reduction % and cytotoxic NK cell % were performed using two-sided Student's t-test. Results aggregated from the top ten fittings based on MSE. Interval bands of 2 s.e. were calculated using a bootstrap of 1000 iterations.

Applications of ABMACT

Augmenting experimental observations by predicting treatment courses

In vivo systems are inherently limited by the frequency and resolution of measurements, often capturing only snapshots of dynamic treatment courses. One key advantage of *in silico* models is their ability to augment and complement existing experimental results, enhancing scale and granularity. ABMACT builds upon this strength by simulating designated durations and inferring subpopulation dynamics that maximally explain laboratory observations. For example, using models for CD19IL15 CAR-NKs, CD19 CAR-NKs, and NT-NKs calibrated on the lymphoma mouse model dataset in Li et al.[56], we projected tumor progression and NK cell population dynamics beyond the endpoint of experimental observation (post mice sacrifice), extending the course to 35 days post-treatment (**Figure 4a-b**).

In addition, ABMACT provided a means to explore the mechanisms underlying heterogeneous experiment outcomes. Our model projected complete tumor elimination by CD19IL15 CAR-NK cells before day 13, whereas in Li et al.[23] most mice showed sustained low tumor burden except before sacrifice except a single mouse exhibiting tumor rebound at the last timepoint. We speculated that the divergence could be due to varying NK cell homing efficacy as previously reported by Ran et al.[57] and Sanz-Orega et al.[58] Keeping a constant total NK cell to tumor cell ratio, we randomly split 10000 tumor cells and 10000 NK cells to simulate varying homing efficacy using local ETR (**Figure 4c**). Reduced homing (local ETR $= 0.12$) resulted in tumor outgrowth, while clearance was still achievable with local ETR ≤ 1.0 but occurred later than day 15 (**Figure 4d**). The averaged tumor progression displayed an initial growth phase, followed by regression and plateau (**Figure 4e**), resembling the rebound pattern in the mouse.

By deconvoluting NK cell populations in the lymphoma and the GBM mouse models, we identified distinct kinetics of engineered NK cells. Notably, cytokine-expressing NK cells, including CD19IL15 CAR-NKs (**Figure 4f**), IL-15 NKs (**Figure 4g**), and IL-21 NKs (**Figure 4h**) exhibited a small peak in cytotoxic NK cell ratios, corresponding to the transition of a subset of cytotoxic NK cells into the vigilant phenotype upon tumor clearance. In contrast, this pattern was not observed in NT-NKs and CD19 CAR-NKs (**Figure S6a-c**). This phenomenon was likely driven by the co-stimulation of endogenous cytokines and residual tumor presence, indicated by cytokine levels and declining tumor-NK cell interaction rate. The cytotoxic NK cell population sustained proliferation while were less prone to exhaustion at the phenotype shift. While the NK cell phenotypes defined in ABMACT are hypothetical and informed by existing studies, the observed NK cell subpopulation trajectories may provide insight into treatment efficacy and warrant further experimental validation.

Figure 4 Plotting the course of cellular treatment using ABMACT.

[Figure 4]

Prediction of tumor and NK population dynamics: (a) Simulated and observed tumor progression in the lymphoma mouse models. (b) Simulated total NK cell population trends in NT-NKs, CD19-CARNKs, and CD19IL15-CARNKs treatment groups in the lymphoma mouse model. Tumor/NK survival calculated by fold changes with respect to the initial tumor population at the start of the simulation. Evaluation of homing efficacy: (c) Schematic of randomizing 10000 tumor cells and 10000 NK cells to 10 sites to simulate varying homing efficacy of NK cells to tumor locations in the CD19IL15-CAR NK cell group. (d) Tumor population fold change by local E:T ratio from simulations of the varying NK cell infiltration. (e) Averaged tumor population fold change. Deconvolution of phenotypes and kinetics: Cytotoxic NK cell ratio, vigilant NK cell ratio, average cytotoxic NK cell proliferation rate, average cytokine level, and tumor-NK cell interaction rate of (f) CD19IL15 CAR-NK cells in the lymphoma model, (g) IL-15 NK cells in the GBM model, and (h) IL-21 NK cells in the GBM model. NK cell subtype ratio calculated with respect to the total NK cell population at each timepoint. Tumor-NK interaction rate calculated by the ratio of tumor cells with co-locating cytotoxic NK cells with respect to the total tumor cell population. Figure 4c created with Biorender.

Discovering key drivers of tumor control through *in silico* perturbation experiments

While numerous CAR engineering strategies aim to enhance NK cells, exhaustive testing of potential designs require significant amount of time and resources. To prioritize the most critical factors influencing tumor control in NK-ACT, we conducted feature importance sensitivity analysis (**Methods**) using *in silico* perturbations in NK cell properties and dosages. The analysis revealed that the effector-to-target ratio (ETR) was the most important feature for accumulated tumor growth, followed by NK cell serial killing capacity (SKC) S_0, death rate d_c, baseline proliferation rate p_c and its decay rate b_{p_c}, and baseline cytotoxicity μ_c (**Figure 5a, Figure S6d**). Increasing ETR from 1:1 to 2:1 drastically shortened the time to tumor clearance, though further increases yielded diminishing returns (**Figure 5b**), aligning with findings previously reported in a CAR-T dosing review study[61]. On the contrary, enhancing SKC and proliferation rates showed a continuous trend of accelerated tumor clearance (**Figure 5c-d**). Parameters contributing to NK cell killing, including S_0, μ_c, CAR effect exponent γ, and cytotoxicity genetic effect coefficient b had a combined feature importance 61% higher than the combined importance of viability parameters (p_c, b_{p_c}, d_c), suggesting that enhancing NK cell killing capacities such as SKC, cytotoxicity, and specific recognition may be more effective than improving their viability in the system.

Assisting treatment decision-making using ABMACT simulation

ACT dose responses often deviate from linear relationships, where excessive dosages may fail to significantly improve treatment efficacy while increasing the risk of toxicity [61]. Designing optimal ACT

treatment regimens is a delicate task, with limited room for repeated experimental testing. ABMACT provides a valuable platform for exploring treatment options and informing clinical decision-making through in-silico simulations. In the lymphoma mouse model simulation, a single dose (1:1 ETR) of NT-NKs at the ETR of 1:1 led to tumor outgrowth (**Figure 2c**). To investigate effective tumor control strategies, we evaluated follow-up treatments with varying dosages, frequencies, timing, and NK cell products using ABMACT simulations (**Figure 5e**). We found that to effectively control tumor outgrowth, it required a higher dose of the same NK cell products (4X) or more effective NK cells such as CD19IL15 CAR-NK cells (1X) (**Figure 5f**). The overall tumor growth was significantly lower in the 4X NT-NK cell group (p-adj < 0.001) and 1X CD19IL15 NK group (p-adj < 0.001) (**Figure 5g**).

Next, we investigated whether administrating the follow-up treatment at different times would result in differential tumor control. One dose (1X) of CD19IL15 CAR-NK cells was administered on day 5, 7, 10, and 14 following the initial treatment, respectively (**Figure 5h**). Earlier intervention contributed to more efficient tumor control (**Figure 5i**) and significantly smaller cumulative tumor burden (**Figure 5j**). Treating refractory tumors with higher doses of more potent ACT products can lead to a more rapid response, and dose fractionation have been used in CAR-T cell therapies and recombinant radiotherapy with CAR-NK cell therapy to mitigate the risks of adverse events associated with high dosages[62,63]. However, it is unclear whether high dosing in NK-ACT is associated with risks[64], and fractioned dosing in NK-ACT alone has not been extensively explored. To examine whether dose fractionation in NK-ACT can effectively control tumors, we simulated follow-up treatment with a total of four doses of CD19IL15 CAR-NK cells administered in one treatment, two treatments, and four treatments (**Figure 5k**). No significant difference in cumulative tumor growth was shown when administrating four doses in one treatment versus splitting to two treatments, but these two treatment strategies resulted in earlier tumor clearance and smaller cumulative tumor burden compared to splitting administrating the four doses over a course of four treatment (**Figure 5l-m**). For aggressive cancer types such as lymphoma, tumor cells escaping NK cell surveillance gain a head-start and undergo exponential growth[65]. When initial treatment fails, higher doses or more potent NK cell products are often required to regain control. The timing of treatment influences response efficacy, while fractionated dosing under calibrated dosage and timing can potentially provide the same treatment benefit as a single higher dose. ABMACT offers a predictive framework for pretesting follow-up treatment strategies, reducing the reliance on extensive laboratory experimentation.

Figure 5 Predicting optimal treatment regimens using ABMACT.

[Figure 5]

Sensitivity analysis: (a) Random Forest regression feature importance of model parameters on tumor progression area under the curve (AUC) measured by mean decrease in impurity (MDI) (**Methods**). Time to tumor clearance by (b) effector-to-target ratio, (c) serial killing capacity, and (d) NK cell baseline proliferation rate. Other parameters and simulation conditions were kept constant. Simulating NK-ACT follow-up treatment: (e) Schema of virtual NK-ACT treatments. Control: NT-NKs were administered at day 0 at an E:T ratio 1:1. 1X NTNK: One follow-up dose (1X) of NT-NK cells was administered on day 7. 4X NTNK: Four follow-up doses (4X) of NT-NK cells were administered on day 7. 1X CD19IL15 CAR-NK: One follow-up dose (1X) of CD19IL15 CAR-NK cells administered on day 7. (f) Simulated tumor progression and (g) accumulative tumor growth (Area under the curve, AUC) of control, 1X NTNK, 4X NTNK, and 1X CD19IL15 CARNK cell treatments. (h) 1X CD19IL15 CAR-NK: One follow-up dose (1X) of CD19IL15 CAR-NK cells was administered on day 5, 7, 10, and 14. (i) Simulated tumor progression and (j) accumulative tumor growth (AUC) of the four treatment groups. (k) 4X1 CD19IL15 CAR-NK: Four follow-up doses (4X) of CD19IL15 CAR-NK cells administered on day 5. 2X2 CD19IL15 CAR-NK: Two follow-up doses (2X) of CD19IL15 CAR-NK cells administered on day 5 and 7 each. 1X4 CD19IL15 CAR-NK: One follow-up dose (1X) of CD19IL15 CAR-NK cells was administered on day 5, 7, 10, 14 each. (l) Simulated tumor progression and (m) accumulative tumor growth (AUC) of the three treatment groups. 10 simulations for each experiment. Interval bands of 2 s.e. were calculated using a bootstrap of 1000 iterations. Figure 5e, h, and k were created with Biorender.

Exploring TME modulation of NK cell efficacy

Beyond intrinsic cell properties and dosage, the TME imposes spatial and metabolic constraints that can significantly module NK cell behaviors. As proof-of-concept (POC) studies, we examined physical barriers in the TME, tissue-aware NK cell motility, and hypoxic stress in the TME (**Methods, Supplementary Materials 5**). First, we used NK cell movement probability and travel distance as surrogates to study the effect of physical barriers in the TME. Restriction to NK cell migration, parametrized by the reduced probability to move (m_N), markedly impaired tumor control (**Figure S7a**). The reduced mobility delayed NK-tumor encounters and allowed tumor outgrowth. In contrast, travel distance within the tumor sites did not substantially affect the time to clearance but influenced the peak tumor population (**Figure S7e**). Next, to capture more realistic cell behavior, we simulated tissue-aware NK cell movement modalities based on the experiment by Dondossola et al.[66] In this POC, non-engaged NK cell agents moved rapidly in the pre-activated state and transitioned to slow-moving after engaging and killing tumor cells (**Figure S7i**), reproducing the reported association between NK cell movement speed and effector function. Finally, we factor oxygen in NK and tumor cell functions to simulate hypoxic conditions induced by oxygen consumption. Under prolonged hypoxia, both NK and tumor population exhibited reduced proliferation, yet the disproportionate loss of cytotoxic NK cells led to tumor rebound (**Figure S7j-l**). Together, the POC studies demonstrate ABMACT's ability to isolate spatial and metabolic factors in the TME, providing insights into how physical barriers and hypoxia can delay NK-tumor interactions, diminish effector persistence, and ultimately compromise therapeutic efficacy. Looking forward, such simulations can be extended to generate testable hypotheses on how modifying the TME may enhance NK cell therapy outcomes.

Discussions

Recent progress in NK cell therapies has highlighted knowledge gaps in their underlying biological mechanisms. While experimental models are indispensable, they are limited in variety, scalability, and resolution. Mechanism-based computational models, particularly ABMs, can provide an efficient and ethical alternative[67].

We developed ABMACT, an agent-based modeling framework incorporating biological rules derived from data and knowledge. By reconstructing the experimental observations from autonomous behaviors of cell agents, ABMACT deconvolutes differential tumor control to cellular and molecular properties. First, simulations of *in vitro* and *in vivo* tumor-immune dynamics revealed that NK cell products with higher viability, cytotoxicity, and serial killing capacity have superior tumor control. These explained the superior efficacy of CD19IL15 CAR-NK cells treating lymphoma and IL21 NK cells treating GBM, while also clarified paradoxical outcomes such as the reduced efficacy of CD19 CAR-NK compared to NT-NK due to activation-induced exhaustion. By integrating scRNA-seq data, ABMACT captured functional genetic heterogeneity in NK cell cytotoxicity. Second, we found the cell-level modeling crucial for capturing NK cell state transitions, functional variations (e.g. NK cell cytotoxicity), and spatial interactions, yielding more accurate and biologically realistic simulations. Third, through systematic in silico perturbations, ABMACT identified the effector-to-target ratio (ETR) as the top determinant to tumor control in addition to the cellular properties mentioned. Virtual dosing studies showed how regimen timing and fractionation can alter tumor rebound and revealed that early intervention was critical to preventing tumor rebound. Finally, compared with other modeling techniques such as ODE, ABMACT outperformed in accuracy, explaining variances in the experimental observations, and stability (**Figure S9, Supplementary Materials 5**). Together, these

capabilities establish ABMACT as both a predictive and mechanistic platform for extracting insights from experiments and informing next-generation ACT strategies.

Parametrizing ABMs depends on data availability and requires balancing computational trackability and modeling accuracy. Despite its strengths, the current version of ABMACT has several limitations. Firstly, as a single-compartment model, ABMACT does not fully account for the immune system and host-level biology. Tumor cells were likely to persist in multiple lymph nodes, and the deviations in simulations of CD19CAR-NKs lymphoma mice model after day 14 likely reflected the inadequate NK cell infiltration to all tumor engraftments or incomplete elimination. Secondly, despite improvement to model accuracy and the ability to capture variations in NK cell cytotoxicity driven by gene and pathway markers, the small sample size of data for feature selection reduced the effect size and might omit key markers. ABMACT can benefit from aggregating multiple studies and establishing genetic markers with higher statistical power. Thirdly, our current model does not consider treatment toxicity, as NK-ACTs have generally been associated with little adverse effects in previous clinical trials[1,5].

Validation against independent datasets has demonstrated ABMACT's generalizability across tumor types. The future work can extend to therapeutic areas beyond NK-ACT and capture more complex spatial interactions. Implemented in the MESA Python framework[68], ABMACT ensures portability, accessibility, and reproducibility. The functional gene feature selection step can be applied to diverse omics datasets, such as scRNA-seq paired with extracellular flux data to characterize cell metabolic states[23]. Other crucial players in anti-tumor immunity, such as macrophages, CD4+ and CD8+ T cells, and dendritic cells can be modeled by modifying and extending the current NK cell agent design. In addition to new molecular features, spatial information such as niches of resistance can be used to model heterogeneity of tumor populations. A proof-of-concept model on hypoxic inhibition of NK cell dynamics is illustrated in **Supplementary Materials 6**. Current 2D modeling in ABMACT reflects the dimensionality and resolution of the experiment data used for calibration. The Moore neighborhood can readily integrate cell coordinates to inform precise positioning of cell populations. High-resolution volumetric data from spatial transcriptomics and multiplexed imaging can be integrated in ABM to provide spatial priors for cell positioning as previously demonstrated[65]. This allows for the representation of more complex tissue structures such as vasculatures, multi-compartmental biology, and patient-specific physiological conditions while avoid artifacts that arise from calibrating 3D modeling against lower-dimensional experimental data. Additionally, coupling ABMs with ODE or PDE models could more accurately capture TME cytokine pharmacokinetics and gene regulatory networks[69]. SDE models can be leveraged to capture cell-level heterogeneities in properties such as proliferation and migration[70]. Such hybrid models can reduce computational costs while maintaining biological relevance, capturing dynamics at both cellular and molecular levels, and extending ABMACT's applicability to broader contexts of immunotherapies. To improve modeling efficiency, surrogate models (e.g. Gaussian process regressors) can accelerate parameter search and prediction[67].

Challenges in ACT trials, including source quality, resistant tumor niches, and comorbidities, also require careful consideration. Source and donor variabilities in NK cell qualities[5,71] can be modeled through modifying cell agent parameters, as demonstrated in the diverging serial killing capacity of optimal cord NK cells (Opt-Cs) and suboptimal cord NK cells (Sub-Cs) in the study by Marin et al.[5] (**Figure S2i**). Prognostic markers and clinical health records, such as serum cytokine concentrations, immune evasive mutations, and comorbidity index, can contribute to both cell agent parametrization and TME specifications. We anticipate the individualized, continuous prediction of treatment outcomes can accommodate variability

beyond patient xenograft models alone. By establishing a bidirectional feedback loop where longitudinal clinical measurements recalibrate model parameters and simulations forecast response trajectories, ABMACT functions as a continuously learning, data-driven system. In chronic disease settings such as cancer, this framework could project disease progression and help identify follow-up windows for optimal treatment opportunities. However, it is important to note that computational models like ABMACT are intended to complement, not replace experimental and clinical studies, and their predictions require validation. By integrating computational insights with experimental findings, ABMACT has the potential to enhance ACT development while maintaining a realistic perspective on its applicability.

In conclusion, ABMACT integrates experimental data and single-cell profiles into mechanistic simulations of NK cell therapies. By quantifying key determinants of ACT efficacy, ABMACT enables in silico prioritization of cell products, laying the foundation for streamlining preclinical development and reducing reliance on animal models, in line with the FDA Modernization Act 2.0[72]. When extended to incorporate patient-specific factors, dosing and fractionation simulations can potentially predict personalized treatment courses to support risk stratification and cohort expansion in future ACT trials. As the first agent-based model dedicated to engineered NK cell therapy to our knowledge, ABMACT sets the stage for computational-experimental codesign of next generation immunotherapies, helping researchers and clinicians anticipate optimization opportunities and risks in ACT therapies.

Methods

In vitro experiment data for model calibration

Cell autonomous growth: Cell counts of NT (n=3) and CD19IL15 CAR-NK (n=3) from day 0 to day 42 were obtained from the cord blood NK cell autonomous growth experiments in Liu et al.[19]. Cells were cultured in vitro without tumor or additional cytokine stimulation[19].

Tumor rechallenge assay: Mean Raji lymphoma tumor population dynamics measured by tumor cell index were obtained from tumor rechallenge assays with cord blood CAR19/IL15 NK cells from optimal cords (Opt-Cs) and suboptimal cords (Sub-Cs) (n=4 each) in Marin et al.[5]. The tumor cell index was measured by the intensity of mCherry fluorochrome, representing the counts of tumor cells[5]. NK cells were challenged against mCherry transduced Raji lymphoma tumor cells at an effector-to-target ratio (ETR) of 5:1 [5]. Tumor cells (100,000 cells) were added every two to three days [5]. Mean glioblastoma tumor population dynamics measured by tumor cell index were obtained from GSC20 tumor rechallenge assays with IL-21 and IL-15 NK cells (n=3 donors each) in Shanley et al.[20]. NK cells were challenged against mCherry transduced GSC20 glioblastoma cells at an E:T ratio of 1:1 [20]. Tumor cells were added every two to three days [20].

Dose-response assay: Mean cytotoxicity profiles of NT, CAR19, CAR19/IL15 NK cells were obtained from the ^{51}Cr-release dose-response assay of NK cell products (n=3 donors) against Raji targets in Li et al.[23]. Cytotoxicity was measured as the percentage of specific lysis of tumor cells relative to targets [23].

Xenograft mice model data for model calibration

Lymphoma

Tumor growth data and scRNA-seq data of NK cells and tumor cells were obtained from the xenograft mice model of Raji lymphoma treated with NK cells in the Figure 2C of Li et al.[23]. The scRNA-seq data are publicly available in Gene Expression Omnibus (GEO) repository at accession number GSE190976. Tumor loads were quantified as average tumor radiance in $p \cdot s^{-1} cm^{-2} sr^{-1}$ [23], which were assumed to be proportional to size of the tumor population (**Figure S3a**). Normalized tumor progression was calculated

by dividing tumor radiances of experiment groups by the mean tumor radiances in the tumor-only control group (**Figure S3b**). NK cells were transfected with retroviral vectors encoding iC9.CAR19.CD28-zeta-2A-IL-15 (CAR19IL15), CAR19.CD28-zeta (CAR19), and IL-15, with non-transduced (NT) NK cells serving as control (n=5 per group) [23]. The xenograft NOD/SCID IL-2Rγ null mice were infused with FFLuc-labeled NK-resistant Raji lymphoma cells (2×10^5 per mouse) on day 0 [23]. NK cells were harvested from each group pre-infusion and on days 7, 14, 21, 28 and underwent scRNA sequencing [23]. Tumor cells were harvested from each group on days 7, 14, 21, 28 and underwent scRNA sequencing [23].

Glioblastoma

Tumor growth data and scRNA-seq data of NK cells were obtained from the xenograft mice model of GSC20 glioblastoma treated with NK cells in Figure 3A of Shanley et al.[20]. The processed scRNA-seq data are publicly available at accession number GSE227098. Tumor loads were quantified as average tumor radiance in $\mathrm{p \cdot s^{-1} cm^{-2} sr^{-1}}$ [20] (**Figure S3c**). Normalized tumor progression was calculated by dividing tumor radiances of experiment groups by the mean tumor radiances in the tumor-only control group (**Figure S3d**). The NOD/SCID IL-2R-null human xenograft mice were intracranially injected 0.5×10^6 patient-derived FFluc-labeled GSC20 tumor cells on day 0 and treated intratumorally with NK cells (n = 3 to 5 per group) at an E:T ratio of 1:5 at day 7 [20].

Blood cancer cell line NK-tumor cell co-culture experiment for independent validation

The tumor cell count and scRNA-seq data of NK cells (syn52600685) were obtained from the 24-hour co-culture experiment of K562 myeloid leukemia cell line in Dufva et al[52]. In the co-culture experiment, NK cells were plated at an ETR of 1:4 with respective tumor cell lines. Samples were harvest at 0,1,3, 6, 12, and 24 hours [52].

Cell agent design

We encoded three NK cell phenotypes: cytotoxic NK cells (N_C), exhausted NK cells (N_E), vigilant NK cells (N_V), along with tumor cells (B, such as B cell lymphoma) in the agent-based model (ABM) using the Python Mesa framework[68] (**Figure 1, Figure S1**). The tumor microenvironment was established in a 2D Moore neighborhood discrete lattice grid to reflect the dimensionality of *in vitro* and *in vivo* data used for calibration and for its simplicity and efficiency in modeling[44]. The Moore neighborhood allows cell movement and interactions in eight directions, reflecting the quasi-random motility of cells. Cell Agents act autonomously by programmed rules and commit to an action when the probability, sampled from a uniform distribution $U(0,1)$, passes a predefined threshold e.g. proliferation rate. For example, Raji lymphoma tumor cells were estimated to have a proliferation rate of 0.455 per day. When at a completion of a cell cycle, a tumor cell agent samples a random number from $U(0,1)$ and compare it with 0.455. If the random number exceeds the threshold, the cell will divide and generate a daughter cell. Cellular properties are encoded as attributes of agents and are inherited by daughter cells from mother cells. The TME was initiated with tumor cells in the center and NK cells in the periphery. We assumed that cell agents followed Brownian motions and modeled cell motility with random walks, while NK cell agents traveled in the direction of the highest tumor concentration due to the chemokine gradient when tumors are present. The specifics of cell agent design are entailed below.

Cytotoxic NK cells (N_C)

A cytotoxic NK cell interacts with a target in three stages: migration, conjugation, and attachment[73]. NK cells can both move freely and migrate towards chemokine or proinflammatory protein gradients[74]. When reaching and recognizing the target, the conjugation phase starts. The NK cell forms an immunological synapse and reorganizes actin cytoskeletons[75,76]. The microtubule organizing center (MTOC) and secretory lysosomes are polarized towards the immunological synapse, followed by lysosome docking and finally the release of cytotoxic molecules into the target cell[75,76]. On ending the conjugation phase, the NK cell begins to dissociate from the target cell irrespective of successful killing, resuming free migration or initiating conjugations with other targets[73]. A cytotoxic NK cell (N_C) is responsible for killing tumor cells. When a N_c cell agent encounters a tumor cell agent, N_C has a probability of p_{kill} to successfully kill the tumor cell, depending on various factors contributing to its cytotoxicity and the tumor cell's ability to evade immune surveillance (p_{evade}). In the process of killing, N_C reduces its serial killing capacity (s), resulting in exhaustion and transformation to the exhausted phenotype (N_E) when s reaches 0. As compared to the other two NK cell phenotypes, N_C cell agents are able to efficiently expand and have the potential to transform to a vigilant phenotype (N_V). In Vanherberghen *et al.*[73], the mean total conjugation and attachment time was measured to be 193 minutes and 235 minutes for lytic and non-lytic events, respectively. Therefore, we considered a four-hour step length ($\Delta T = 4hr$) for the ABM to approximate the time for cytotoxic NK cells moving toward tumor cells and exert killing.

Cytotoxic killing activity

To reduce parameter search space for NK cell cytotoxicity in ABM, we performed initial estimation of relative baseline cytotoxicity of CAR19IL15 NK cells, CAR19 NK cells, and NT NK cells using the dose-response data from the ^{51}Cr-release assay of NK cell products against Raji targets in Li et al.[23]. We applied the following dose-response Emax model:

$$\mathrm{E(y)} = \frac{\mathrm{E_0}}{1 + \left(\frac{\mathrm{R} * \mathrm{x_g}}{\mathrm{k_{50}}}\right)^{\mathrm{m}}} \tag{1}$$

where $\mathrm{x_g}$ denoted the average relative NK cell cytotoxicity of the group g, $\mathrm{E_0}$ denoted the baseline death percentage (cytotoxicity) of tumor cells at ratio = 0, R denoted the effector:target ratio, $\mathrm{k_{50_g}}$denoted the half-maximum relative average NK cell cytotoxicity of the group g, and m denoted Hill's coefficient (shape parameter). We assumed $\mathrm{E_0}$ is constant across groups given the same Raji tumor cells used in experiments. The nonlinear least squares estimation was performed using the least_squares function of the Python package scipy[77]. Three types of loss including "linear", "soft_l1", and "cauchy" were compared to select parameters with minimum loss.

We constructed the probability of killing a tumor cell upon contact $\mathrm{p_{kill}}$ with reference to the cytotoxicity function in [41]. p_{kill} is a function of baseline cytotoxicity $\mathrm{c_{NK}}$, gene effects $\mathrm{G_{NK}}$, CAR engineering effect γ, and the tumor cell's probability to evade recognition $\mathrm{p_{evade}}$:

$$\mathrm{p_{kill}} = \left[\frac{1.0}{1.0 + \exp\left(-\left(\mathrm{c_{NK}} + \mathrm{G_{NK}}\right)\right)}\right]^{\gamma} * \left(1 - \mathrm{p_{evade}}\right) \tag{2}$$

where $\mathrm{c_{NK}} \sim \mathrm{truncN}(\mu_c, {\sigma_c}^2)$, $\mathrm{G_{NK}} = \tanh\left(\mathrm{b}\sum_{\mathrm{i}=1}^{\mathrm{k}} \beta_\mathrm{i} g_\mathrm{i}\right)$, and b is the overall NK cell cytotoxicity genetic effect coefficient to ensure reasonable scaling. The first part of the formula consists of an exponentiated sigmoid function that accounts for the nonlinear relationship between p_{kill} and NK cell cytotoxicity and

genetic effects. The initial value of NK cell baseline cytotoxicity μ_c was estimated based on the dose-response data from the ^{51}Cr-release assay of NK cell products against Raji targets in Retzlaff et al.[23] and refined using global search (**Supplementary Materials 1**). The RNA expressions of significant genes and pathways associated with NK cell cytotoxicity **g** and respective coefficients **β** were obtained from the cross-lagged LME model M_{NK}.

Characterize NK cell proliferation kinetics

NK cells require extrinsic stimulations to expand and persist. Studies have shown that the presence of cytokines such as IL-15 and tumor antigens enhances NK cell expansion[5,19,23]. Without exogenous stimulation, NK cell expansion could not be sustained, and the population start to wane in one to two weeks[78]. In the cell autonomous growth experiment in Liu et al.[19], IL-15-expressing CAR-NK cells sustained higher population than NT NKs, although the effect of IL-15 stimulation on NK cell proliferation and survival gradually reduced due to system clearance[19].

Therefore, we hypothesized that the endogenous cytokine expression such as IL-15 in CAR-NK cells is crucial for population expansion in addition to tumor antigen stimulation. Using an exponential form and Hill's equation to describe the nonlinear dependencies between cytokine concentration and cell proliferative property[79], we proposed a cytokine-dependent model (CM) for computing the proliferation rate of IL-15-expressing NK cells as follows.

$$p_c^*(t) = p_c \exp\left(w - b_{p_c} t\right), \tag{3}$$

$$w = k_B * \frac{c_{(i,j)}^{\gamma_2} + \delta}{c_{(i,j)}^{\gamma_2} + c_{50}^{\gamma_2} + \delta} \tag{4}$$

Initial ranges and default values of hyperparameters were determined using linear programming of biological constraints. p_c is baseline cytotoxic NK cell proliferation rate, $c_{(i,j)}$ is the dimensionless cytokine concentration level in the neighboring region (i,j), c_{50} is the half-maximum cytokine level. γ_2 is the Hill's equation exponent, b_{p_c} is the natural decay rate parameter of proliferation rate, t is cell age, and δ is a small constant for keeping w nonzero. $k_B = \frac{B_{(i,j)}^{\gamma_1} + \delta}{B_{(i,j)}^{\gamma_1} + B_{50}^{\gamma_1} + \delta}$ is the tumor stimulation effect considering tumor count $B_{(i,j)}$ in the neighborhood (i,j), half-maximum tumor load B_{50}, and a Hill equation exponent γ_1. k_B is a constant in the context of NK cell autonomous growth as tumor cells are absent and kept to the default value. We considered a half-life of 2.5hrs for IL-15[80]. At every step of the ABM, the real-time cytotoxic NK cell proliferation rate p_C' was sampled from a $\mathrm{truncN}(p_c^*(t), {\sigma_{\mathrm{p_C}}}^2)$ distribution.

CM is compared to a vanilla model (VM) of $w = 0$ and a b invariant across groups. The first 70% of data were used for fitting and the remaining for testing. Parameters c, γ_2, b were globally searched to minimize mean squared errors (MSE) between simulated and observed population fold change with respect to the initial cell counts. The characterization of NK cell proliferation model is performed on the autonomous growth kinetics of cord blood (CB) CAR-NK and NT-NK cells using measured cell counts data from [19]. Results are provided in **Supplementary Materials 1**.

Exhausted NK cell (N_E) and characterize NK cell exhaustion process

In adoptive cell therapy, NK cell serial killing capacity (SKC) can be modulated by its CAR engineering[23], source quality[5], gene editing[22], and cytokine stimulation[81]. Once a cytotoxic NK cell exhausts, it will no longer be able to kill tumor cells but can remain in the system in the presence of tumor antigen. We focused on aspects of NK cell exhaustion due to loss of ability to secret cytolytic granules and impaired cytotoxicity due to dysregulated inhibitory signals. The former was quantified as the serial killing capacity s, and the latter was modeled by a link function between the probability of killing a tumor cell upon contact, p_{kill} and RNA expression of genes found to be significantly associated with NK cells' tumor control ability based on the LME modeling. Bhat et al.[81] demonstrated that one NK cell was able to kill four to six tumor cells in 16 hours. However, the experiment was limited in duration to thoroughly measure the maximum SKC. To date, the exhausted NK cell phenotype can only be determined functionally using NK cell rechallenge assay. To fill the gap of mathematical models of NK cell exhaustion, we hypothesized that NK cell exhaustion could be deconvoluted as the reduction of serial killing capacity and impaired killing capability. We encoded an NK cell initial SKC parameter S_0, which reduced as NK cell killed targets (event denoted as I_{kill}). The following Exhaustion Models (EM) are proposed.

Exhaustion Model 1 (EM1):

NK cell exhaustion can be primarily described by the linear reduction in SKC. A cytotoxic NK cell (N_C) transformed to an exhausted NK cell (N_E) when its current SKC reached zero.

$$s = S_0 - \sum I_{kill} \tag{5}$$

Exhaustion Model 2 (EM2):

In addition to the linear reduction in SKC, interactions with tumor cells increase the inhibitory signaling in NK cells such. Given that exhaustion markers LAG3 and PDCD1 were found to be significantly associated with NK cell cytotoxicity based on the cross-lagged LME model M_{NK}. We model the exhaustion process as:

$$s = S_0 - \sum I_{kill} \tag{6}$$

$$\boldsymbol{x}'_{G_{exh}} = \boldsymbol{x}_{G_{exh}} + \sum I_{kill} \tag{7}$$

where $\boldsymbol{x}_{G_{exh}}$ is the vector of RNA expression of exhaustion marker genes $G = \{LAG3, PDCD1\}$, which further updates NK cells' killing probability p_{kill}.

Exhaustion Model 3 (EM3):

Increased expression of exhaustion markers could in turn regulate the synthesis and secretion of cytolytic granules. We used an exponential function to link Hill equations of exhaustion markers to the reduction of serial killing capacity.

$$s = S_0 - \sum I_{kill} e^{\gamma_{exh}} \tag{8}$$

$$\gamma_{exh} = \sum \frac{\boldsymbol{x}_{G_{exh}}}{\boldsymbol{x}_{G_{exh}50} + \boldsymbol{x}_{G_{exh}}} \tag{9}$$

$$\boldsymbol{x}'_{G_{exh}} = \boldsymbol{x}_{G_{exh}} + \sum I_{kill} \tag{10}$$

We compared the three EMs by fitting to tumor rechallenge assay in [5] and selected the model with the smallest MSE loss. Results are provided in **Supplementary Materials 1**.

Vigilant NK cells (N_V)

Several studies have demonstrated that NK cells exhibit functions previously only available among cells of the adaptive immune system, including the cell memory[49,78]. Homeostatic proliferation drives NK cells to transform into a dormant, sustained phenotype with preserved effector function and self-renewal potential that can live in the host for prolonged time[48,49,82–87]. To differentiate such NK cells before and after the second viral or pathogen challenge, we termed the former as vigilant NK cells ($\mathrm{N_V}$) and the latter as memory-like NK cells. In ABMACT, upon local tumor clearance ($B\_$), cytotoxic NK cells exposed to tumors can transform to vigilant NK cells ($\mathrm{N_V}$) at a probability k_{B-}. The vigilant cluster had a lower proliferation rate p_V and death rate d_V to sustain a small population in the host. A proportion of the vigilant NK cells are capable of exhibiting recall upon a second tumor stimulation (event denoted as B_+ when tumor cells are present in the neighborhood) and convert back to cytotoxic NK cells at a probability k_{B+}.

Tumor cells (B)

Malignant cells are characterized by uncontrolled growth and immune evasion[88]. B-cell non-Hodgkin lymphoma was characterized to have a medium proliferation rate ranging from 0.15 per day to 0.80 per day in indolent to highly aggressive types[89]. Glioblastoma was estimated to have a medium proliferation rate of 0.022 per day using patient MRI data[90]. The tumor cell agents (e.g. B cell lymphoma, glioblastoma) are modeled to be highly proliferative with a minimum likelihood of apoptosis. Proliferation rates p_B can be specific to cell lines, host conditions, and other factors. Proliferation rates used in modeling were estimated using tumor-only bio-illuminance data from the lymphoma[56] and GBM[20] mouse models using the following ODE model:

$$\frac{\mathrm{dB}}{\mathrm{dt}} = \mu\left(1 - \frac{\mathrm{B}}{\mathrm{B_{max}}}\right)\mathrm{B} \tag{11}$$

where B is average tumor radiance, which is a surrogate for tumor size, μ is tumor cell proliferate rate in $\mathrm{day^{-1}}$, and $\mathrm{B_{max}}$ is the equivalent average radiance of growth-limiting tumor size (**Supplementary Materials 1**). To account for immune evasion, we assumed tumor cells can evade CAR-NKs by downregulating CAR target and gain mutations over generations. In the lymphoma mouse model, CD19 expressions are sampled and randomly assigned to tumor cell agents to represent tumor heterogeneity. We assumed tumor cells has a probability of gaining immune resistant mutation p_{mutate} of 0.001[91], which is added to the probability of evading NK cell cytotoxic killing p_{evade}. In models with specific CAR targets such as anti-CD19, the expression of the target in tumor cell agents modifies p_{evade}. For example, p_{evade} of tumor cells expressing high CD19 is proportionally reduced by a constant scaling factor. In addition to proliferation, death, mutation, a tumor cell agent is able to move to neighboring grids at every model step with a probability $\mathrm{m_B}$.

Integrate functional genetic effects in cell agents

Single-cell RNA sequencing data processing

Longitudinal scRNA-seq data of NK cells and tumor cells were obtained from GSE190976 and processed as described in Supplementary Materials of Li *et al.*[56]. GOBP gene set density scores (GSDS) were calculated using R package "gsdensity"[92]. Pre-infusion scRNA-seq data of IL-15 and IL-21 NK cells[20] were obtained from GSE227098 in Shanley et al. [20].

Feature selection using linear mixed effects modeling

NK cell lysis killing is tightly regulated by a repertoire of activating surface receptors inhibitory receptors such as Fc receptor FcγRIIIa (CD16), NKG2D, and KIR2DL1[73,76,93]. To understand the molecular features underlying NK cells anti-tumoral capability, we performed feature selection on a literature-curated list of 112 NK cell genes and 5 GO Biological Process (GOBP) pathways[23,55,76,94–97] (**Supplementary Materials 2**) that regulate NK cell activation, inhibition, OXPHOS, proliferation, survival, cytotoxicity, regulatory function, and memory function.

To select significant genes and pathways and quantify their effects on NK cell cytotoxicity, we applied linear mixed-effects (LME) modeling to paired scRNA-seq data of NK cells and tumor radiance data from the lymphoma mouse model in Li et al.[56] using R package lme4[98]. We assume that gene-expression patterns in NK cells are associated with function of NK cells and their anti-tumor control effecting tumor size at the next timepoint, as NK cells required tumor antigen stimulation to sustain and might have drastically waned at the time of sample collection if tumors were cleared. Tumor loads were at D28 were excluded due to cell count scarcity. The cross-lagged LME model for NK cells, M_{NK}, included random intercept effects for time and group to consider temporal and inter-group variations. $\mathrm{M_{nk}}$ was defined as:

$$\mathbf{Y} = \mathbf{X_{NK}}\boldsymbol{\beta}_{\mathbf{NK}} + \mathbf{Z_{NK}}\mathbf{u_{NK}} + \boldsymbol{\epsilon}_{\mathbf{NK}}, \tag{12}$$

where $\mathbf{Y} = (\mathrm{y_k})_{\mathrm{K}}$ are means of tumor radiance in unit of $\mathrm{p \cdot s^{-1}cm^{-2}sr^{-1}}$ across all mice in the k-th group at $t_2,\ldots,t_T$, $k \in \{1, \ldots, K\}$. $\mathbf{X} = \left(\mathrm{x_{kig}}\right)_{\mathrm{K*I*G}}$ are gene expressions of the g-th gene of the i-th cell in the k-th group at a timepoint $t_2, \ldots, t_{T-1}$, $g \in \{1, \ldots, G_i\}, i \in \{1, \ldots, I_k\}$. $\boldsymbol{\beta} = \left(\beta_{\mathrm{g}}\right)_{\mathrm{G}}$ are regression coefficients of fixed effects for the g-th gene. $\mathbf{Z} = \left(\mathbf{Z_j}\right)_{\mathrm{J}}$ are random effects for time and group, $\mathrm{j} \in \{\mathbf{t}, \mathbf{k}\}$, . $\mathbf{u} = \left(\mathrm{u_j}\right)_{\mathrm{J}}$ are random effects regression coefficient for the j-th random effect, $\mathrm{u_j} \sim \mathrm{N}(0, \mathrm{G_{u_j}})$ and $\mathrm{G_{u_j}}$ is the covariance matrix**,** and $\boldsymbol{\epsilon} = (\epsilon_{\mathrm{ki}})_{\mathrm{K*I}}$: random error for the i-th cell in the k-th group, $\epsilon_{\mathrm{ki}} \sim \mathrm{N}(0, \sigma_{\mathrm{e}}^2)$. Notations in the format $(X_i)_I$ denotes data X of the i-th element in a matrix I, and I can be multi-dimensional.

We used a two-step approach for model variable selection and fitting. In the first round of fitting, single covariate LME models were fitted for each gene and GOBP. Significant covariates were retained in the final model based on p values adjusted for multiple testing. LME models were fitted using restricted maximum likelihood and Nelder-Mead optimizer given small sample sizes. Due to overlaps between genes selected based on literature reviews and relevant GOBP gene sets, we compared models with and without GOBP gene sets and the null model with only random effects using Akaike information criterion (AIC) and Bayesian information criterion (BIC). The LME model with coefficients in **Supplementary Data 1** had the smallest AIC and BIC. We currently considered a total of 117 genes and GOBPs for NK cell genetic effect model, which can be further expanded to include additional genes and pathways. As the number of genes and pathways of interest exceeded the number of observations, this approach allows efficient dimensionality reduction while controlling for false discoveries.

Integrate functional genetic effects in cell agent cytotoxicity

Fixed effects regression coefficients of significant genes and GOBP pathways, $\boldsymbol{\beta}_{\mathbf{NK}}$**,** were multiplied with -1 to further parametrize cytotoxic NK cell agents' probability of killing a tumor cell upon contact, p_{kill}, as described in Methods section "Cytotoxic killing activity." In the lymphoma model, the scRNA-seq data at pre-infusion were sampled and randomly assigned to cytotoxic NK cell agents for respective experiment groups. In the GBM model, the scRNA-seq data at pre-infusion were sampled and randomly assigned to

cell agents for respective NK cell groups. The expressions multiplied with coefficients derived above and contributed top_{kill}.

Tumor cell viability model M_{TM}

In addition to M_{NK}, we also built an LME model for tumor cells with scRNA expressions of tumor cells and tumor radiance. Tumor cells are intrinsically programmed to proliferate and survive[88]. We focused on 17 GOBPs governing tumor cell proliferation, cell cycle regulation, and apoptosis. We also included *HLA-E, HLA-C, HLA-B, HLA-A, HLA-F, HLA-G, HLA-DOA, HLA-DOB* for immune recognition[99], *BRAF*, *NRAS*, *KIT, MAPK2* for uncontrolled cell growth[100], *ERBB4, GRIN2A*, and *GRM3* for tumor progression, *RAC1* and *PREX2* for cell motility and metastasis[101,102], *HIF1AN*, *HIF1A-AS1*, *HIF1A*, and *HIF1A-AS2* for hypoxia response[103], and *VEGFC, VEGFA, VEGFD*, and *VEGFB* for angiogenesis and metastasis[104]. The complete list is provided in **Supplementary Data 1**.

To select significant genes and pathways and quantify their effects on tumor viability, we applied an LME model, $\mathrm{M_{TM}}$, to paired scRNA-seq data of tumor cells and tumor radiance data from the lymphoma mouse model[56] using R package lme4[98]. In $\mathrm{M_{TM}}$, we proposed that tumor viability was associated tumor scRNA-seq data at the current time point. $\mathrm{M_{TM}}$ was defined as:

$$\mathbf{Y} = \mathbf{X_{NK}}\boldsymbol{\beta}_{\mathbf{NK}} + \mathbf{Z_{NK}}\mathbf{u_{NK}} + \boldsymbol{\epsilon}_{\mathbf{NK}}, \tag{13}$$

where $\mathbf{Y} = (\mathrm{y_k})_{\mathrm{K}}$: mean average tumor radiance in unit of $\mathrm{p/s/cm^2/sr}$ of mice in the k-th group, $\mathbf{X} = \left(\mathrm{x_{kig}}\right)_{\mathrm{K*I*G}}$: gene expression of the g-th gene of the i-th cell in the k-th group, $\boldsymbol{\beta} = \left(\beta_{\mathrm{g}}\right)_{\mathrm{G}}$: fixed effects regression coefficient for the g-th gene, $\mathbf{Z} = \left(\mathrm{Z_j}\right)_{\mathrm{J}}$: random effects for time and group, $\mathrm{Z_j} = (\mathrm{t}, \mathrm{k})$, $\mathbf{u} = \left(\mathrm{u_j}\right)_{\mathrm{J}}$: random effects regression coefficient for the j-th random effect, $\mathrm{u_j} \sim \mathrm{N}(0, \mathrm{G_{u_j}})$ and $\mathrm{G_{u_j}}$ is the covariance matrix, and $\boldsymbol{\epsilon} = (\epsilon_{\mathrm{ki}})_{\mathrm{K*I}}$: random error for the i-th cell in the k-th group, $\epsilon_{\mathrm{ki}} \sim \mathrm{N}(0, \sigma_{\mathrm{e}}^2)$.

Simulation

Evaluation metrics

To make simulation data comparable to experimental observations, tumor progression in simulations and in experimental observations were normalized by tumor-only control measurements, respectively. The simulated normalized tumor progression was calculated as $r_{sim} = \frac{T_g}{T_{control}}$, where $T_g(t) = \frac{N_g(t)}{N_0}$ was tumor cell agent count at timepoint t in group g normalized by tumor cell agent count at timepoint 0, $T_{control}(t) = \frac{N_{control}(t)}{N_0}$ was tumor cell agent count at timepoint t in the tumor-only control group normalized by tumor cell agent count at timepoint 0. The observed normalized tumor progression was calculated as $r_{obs} = \frac{V_g}{V_{control}}$, where $V_g(t)$ is the average tumor radiance in $\mathrm{p \cdot s^{-1}cm^{-2}sr^{-1}}$ at timepoint t in group g and $V_{control}(t)$ is the average tumor radiance in $\mathrm{p \cdot s^{-1}cm^{-2}sr^{-1}}$ at timepoint t in the tumor-only control group. Simulation results were evaluated on normalized tumor progression r_{sim} and r_{obs} using the total loss L_{total} calculated as follows:

$$L_{total} = L_{MSE} + L_{MAE} + \Delta_{AUC} + 1 - R^2 \tag{14}$$

where $L_{MSE} = MSE(r_{sim}, r_{obs})$ is the mean squared error (MSE) loss, $L_{MAE} = MAE(r_{sim}, r_{obs})$ is mean absolute error (MAE) loss, $\Delta_{AUC} = |AUC(r_{sim}) - AUC(r_{obs})|$ is the difference between the area under the curve (ΔAUC) in simulated and observed data, and R^2 is coefficient of determination calculated by scikit-

learn function r2_score[105]. Each component was chosen to capture complementary aspects of model performance. MSE captures large deviations between simulated and observed tumor trajectories, while the MAE provides a robust measure less influenced by outliers. ΔAUC compares the integrated tumor burden over time. R^2 quantifies the proportion of variance explained by the model; including $1 - R^2$ ensures penalization of poor overall fit even when pointwise errors are small. Together, these terms balance sensitivity to local fluctuations, robustness to noise, and fidelity to global tumor control dynamics.

Simulation initiation

The simulations were initiated with a 2D discrete Moore space. A tumor niche was initiated with 1000 tumor cell agents in a 50 by 50 grid, corresponding to a spatial density that supported biologically realistic encounter rates while avoiding overcrowding or excessive sparsity. The number of NK cells varied depending on the effector-to-target ratio (ETR). We evaluated alternative densities and found that both lower and higher initial occupancies (≤ 0.2 cell/grid or ≥ 1.2 cell/grid) reduced fitting accuracy given the same ETR of 1.0 (**Supplementary Materials 3.1**). Because of the intra-tumoral administration of NK cells in the GBM mouse model, we assumed no loss of NK cells in infusion and an ETR of 1:5 for all three groups, same as the mouse experiment setup. Simulation data were aggregated to compute the mean and standard deviation.

Calibration

The large parameter space of the proposed model requires both literature-informed parameter setting and multi-stage parameter calibration. To reduce the high computation demand of parameter search of ABM, we iteratively optimized the following hyperparameters prior to more granular parameter search for parameters most pertinent to NK cell efficacy. Hyperparameters for NK cell proliferation function, including Hill's equation exponent of tumor antigen effect (γ_1), Hill's exponent of cytokine effect (γ_2), half-maximum tumor load (B_{50}), and half-maximum of cytokine's effect (C_{50}) are calibrated on CAR19IL15 NK cell and NT NK cell autonomous growth data from Liu et al[19]. Proliferation rate (p_B) and death rate of tumor cells (d_B) were estimated based on lymphoma and glioblastoma studies by Li et al.[23] and Shanley et al.[20], respectively. Three hyperparameters for tumor cells were fixed as constant based on literature-informed assumptions. Tumor cell movement probability (m_B) and speed (v_B) were set to be small positive constants based on the assumption that tumor cells have relatively lower mobility than NK cells. Tumor mutation rate p_{mutate} was set as a small positive to represent tumor cells' capability to gain immune resistant mutation[91]. After setting these parameters, number of tumor cells n_{tumor}, number of initial cytotoxic NK cells n_{NK}, NK cell baseline proliferation rate p_c, NK cell death rate d_c, NK cell proliferation decay rate b_{p_c}, NK cell serial killing capacity (SKC) S_0, and baseline cytotoxicity μ_c are varied to search for optimal fitting.

In lymphoma mouse model, data points at day 0, 7, and 14 post-engraftment (equivalent to day 7 and 14 post-infusion) were used for model calibration. The assumption that engraftment occurred seven days post infusion was based on the comparable tumor radiance in mouse models at day 7 (Figure 2C in Li et al.[56]). For the lymphoma mouse model, data points after post-engraftment day 14 (equivalent of post-infusion day 21) were removed due to lack of data points for the Raji control group. Each simulation in lymphoma autonomous growth, rechallenge assay, and mice model simulations was repeated 30 times. In GBM mouse model, data points at day 14, 22, and 37 after intra-tumoral injection were used for model calibration. Each simulation in the GBM mouse model was repeated 5 times due to computation time constrain.

We estimated the ETR by selecting the ETR that minimize the total loss across groups. The remaining parameters were selected by minimizing total loss under the ETR. The top 10 parameters with minimum total losses were also reported. The lymphoma and GBM ABMACT model parameters are listed in **Table 1**.

Table 1 Model parameters.
[Table 1]

Independent validation

We tested the calibrated non-transduced NK (NT-NK) cell model using the K562 cell line co-culture experiment from Dufva et al[52] that were not used in the calibration process. Genetic features of NT-NK cells and tumor cells are obtained from scRNA-seq data in Dufva et al.[52] under the Synapse accession number syn52600685. K562 myeloid leukemia cell line coculturing with NT-NK cells was simulated using the calibrated ABMACT. GSEA scores are calculated using fgsea[106] in R. Simulations followed experiment setup of a 1:4 effector-to-target ratio (ETR) and an estimated density of 0.5 million tumor cells per ml. 3,125 virtual tumor cells and 782 virtual NT-NK cells were randomly placed in a 50 by 50 Moore's grid with each grid cell representing a $50\mu m$ by $50\mu m$ space. The simulations followed the co-culture time of 24 hours, during which NT-NK cells autonomously interacted with tumor cells.

Feature importance sensitivity analysis

Aggregating simulation data from in silico perturbation experiments of ABMACT, we trained a Random Forest Regressor (RFR) using scikit-learn[105] to evaluate the importance of model parameters on accumulated tumor growth and prediction accuracy. Tumor growth was measured by the area under the curve (AUC) over a 35-day simulation period. Prediction accuracy was measured by MSE between simulated data and observed experiment data in the xenograft lymphoma mice model in Li et al.[56]. Feature importance was evaluated by the mean decrease in impurity (MDI) and permutation importance (PI). MDI measures the information gain of features in predicting outcomes. In the case of predicting a continuous outcome variable, MDI measures the reduction in MSE when splitting a variable at a tree node.[107]. PI measures the reduction in the model accuracy score when randomly shuffling a feature's value, overcoming the potential biases of MDI for highly variable features[108]. Sensitivity analysis simulations were repeated 10 to 30 times.

To evaluate the robustness of model parameters, we assessed the variance explained by the sensitivity analysis parameters using linear regression model and type II ANOVA test. To test robustness to sampling variability, we subsampled 80% of the sensitivity analysis dataset and refitted the Random Forest Regressor 30 times. To evaluate interdependencies between model parameters, we conduct global sensitivity analysis by simulating CD19IL15CAR-NK cell lymphoma model with $\pm$ 10% variations and analyzed the results using Spearman's correlation.

Detailed sensitivity analyses are provided in **Supplementary Materials 4**.

Uncertainty estimation

Coefficient of variation

We followed the approach by Nikishova et al[109] and evaluated simulation stability using coefficient of variation ($CV = \sigma/\mu$) on accumulated tumor progression, measured by normalized area under the curve (AUC), of ABMACT calibrated on the lymphoma model by Li et al.[23] (**Supplementary Materials 3.2**). Each simulation was repeated 10 times with the calibrated parameters over 35 simulation days. Normalized tumor progression AUC was calculated by first dividing tumor cell agent population counts in the treatment group by the mean tumor population count in the tumor-only control group and then averaging over time. The mean and standard deviation were calculated over repeats for each treatment group.

Simulation-based inference parameter distribution estimation

We used a simulation-based inference workflow by Boelts et al.[110] to create surrogate models and estimate parameter distributions. Using the sbi Python package by Boelts et al.[110] and the method by Papamakarios & Murray[111], we trained a posterior estimation model on simulation lymphoma model data generated by ABMACT. In total 11 parameters were evaluated, including ETR, cytotoxic NK cell proliferation rate p_C, NK cell migration rate m_N, NK cell death rate d_C, NK cell baseline cytotoxicity μ_C, NK cell serial killing capacity s, CAR effect coefficient γ, NK cell genetic effect coefficient b, and three hyperparameters for NK cell proliferation rate (tumor load half-maximum B_{50}, cytokine concentration half-maximum c_{50}, and decay rate b_{p_C}). The observations to were summarized to tumor population fold change normalized to tumor only control at day 0, 7, 14 post-engraftment. To estimate posterior distributions of parameters, normalized tumor progression in the mice models of the NT, CAR19, and CAR19IL15 NK cell groups in Li et al.[23] were given to the surrogate model and 1000 posterior samples of the parameters were drawn. Mean and standard deviation of posterior distributions are reported in **Supplementary Data 2**.

Benchmarking with ordinary differential equations

To benchmark ABMACT, we compare it with the commonly used ordinary differential equation (ODE) models on the lymphoma mice model dataset using the total loss metrics (L_{total}) specified in "Evaluation metrics" (**Supplementary Material 3.4**). ABMACT and ODE models were calibrated on the same xenograft lymphoma mice model data in Li et al. [56]. The ODE fitting results are provided in **Supplementary Data 3**.

The ODE models are adapted from the approach in Kirouac et al.[50] and constructed with consideration of NK cell cytotoxicity and transitions between phenotypes as follows:

$$\frac{dB}{dt} = \mu_B B - p_{k_g} N_c \tag{15}$$

$$\frac{dN_c}{dt} = \mu_g \left(\frac{B^{m_1}}{B50^{m_1} + B^{m_1}}\right) N_c - d_g N_c - \left(1 - \frac{s_g}{S_g}\right) N_c - p_v \left(\frac{1}{1 + B^{m_2}}\right) N_c \tag{16}$$

$$\frac{ds_g}{dt} = -p_{k_g} + \mu_g \left(\frac{B^{m_1}}{B50^{m_1} + B^{m_1}}\right) S_g \tag{17}$$

$$\frac{dN_e}{dt} = \left(1 - \frac{s_g}{S_g}\right) N_c - d_g N_e \tag{18}$$

$$\frac{dN_v}{dt} = p_v\left(\frac{1}{1+B^{m_2}}\right)N_c - d_v N_v \quad (19)$$

Here, tumor cell population B had proliferation rate μ_B. Cytotoxic NK cells N_c could kill tumor cells at a probability of p_{k_g}. Different NK cell products possess varying properties, the subscript g denotes parameters specific to NK cell group g. N_c population proliferated at a baseline proliferation rate μ_g and modified by the presence of tumor antigen. The modification effect of tumor antigen was represented by the Hill's function $\frac{B^{m_1}}{B50^{m_1}+B^{m_1}}$, where $B50$ was the half-maximum population count of tumor cells and m_1 was Hill's exponent. N_c died at a probability of d_g. The exhaustion of cytotoxic NK cells was modelled by the reduction of average serial killing capacity of the population as $\left(1-\frac{s_g}{S_g}\right)N_c$, where s_g measured the average serial killing capacity of N_c, and S_g was the maximum serial killing capacity. s_g was reduce by the average killing rate p_{k_g} and increased by the generation of new cytotoxic NK cells. When tumor cells were cleared, N_c could also transform to the vigilant phenotype N_v at a probability p_v. In the modifier $\frac{1}{1+B^{m_2}}$, m_2 was a large enough constant so that the transformation only occurred after B approached 0. N_e denoted the number of exhausted NK cells. d_v was vigilant NK cells' death rate.

Parameter fitting was obtained by minimizing the total loss L_{total} of normalized tumor progression between ODE prediction and experimental data in the lymphoma mouse model by Li et al.[23] The total loss included MSE, MAE, difference between simulated and observed tumor progress area under the curve Δ_{AUC}, and coefficient of determination R^2. Random parameter initialization and fitting were performed and repeated 30 times. The top 10 best fitting with the smallest loss were selected.

Proof-of-concept models

TME physical barriers

Spatial constraints on NK cell anti-tumoral efficacy can be reflected by NK cell infiltration. Direct quantification of physical barriers would require new experimental measurements and specialized algorithms, which would add complexity to the model. As a pragmatic alternative, we introduced two surrogate measures of physical barriers to NK cell infiltration and evaluated their impact on accumulated tumor growth using the area under the curve (AUC). We performed simulations on 1) varying NK cell movement probability (m_N), and 2) varying distances between NK cell infiltration border and tumor seeding area under the setting of the CAR19IL15NK cell treatment of lymphoma mice models in Li et al.[23] (**Supplementary Materials 5.1**)

Migration restriction: Resistance from physical barriers such as extracellular matrix was modeled by varying the NK cell migration probability (m_N). The original calibrated model used $m_N = 0.9$, which was reduced to 0.7, 0.5, and 0.3 to simulate progressively restricted migration.

Migration distance: The tumor seeding area was varied to represent different distances that NK cells must travel to reach tumor cells. Distance was quantified as the ratio between tumor seeding area diameter and the simulation space width. Relatively to the control setup, the distance was increased by 5% and 15% from the original model setup (control). All other parameters were kept consistent with the calibrated model.

NK cell movement dynamics

We developed a preliminary NK cell agent model that takes into consideration tissue density and movement modality (**Supplementary Materials 5.2**). We introduced a modifier function to NK cell movement speed v_N based on TME density as follows:

$$v'_N = v_N(1 - A_{cell}/A_{max}),$$

where A_{cell} is the total cell space occupied and A_{max} is the maximum capacity. NK cell movement will be reduced in dense areas to model the difference in movement in liquid tumors versus solid tumors such as glioblastoma. In addition, based on the experiment by Dondossola et al[66], NK cells displayed movement modalities that are associated with their effector function. Non-engaged NK cells showed an average moving speed of $5.83 \pm 0.86\ \mu m/min$ and are less prone to cytotoxic killing, while engaged NK cells showed an average moving speed of $2.71 \pm 0.71\ \mu m/min$ and more prone to cytotoxic killing. Based on this experiment, we modified the movement function of NK cell agents.

Hypoxic condition

To demonstrate how niches of resistance can suppress NK cell activities, we implemented a proof-of-concept model for hypoxic regions created tumor oxygen competition and tracked NK cell dynamics (**Supplementary Materials 5.3**). Default oxygen concentration of 1.35e-8ml/grid and standard oxygen consumption rate of 2.16e-9ml/cell/hr per unit activity follows the ABM simulation setup in the study by Jalalimanesh et al.[112] Pathological hypoxia is defined as the oxygen level reaching 20% of the default oxygen concentration[113]. We implemented the following rules: 1) NK cell agents exhibit reduced proliferation and cytotoxicity under hypoxic conditions; 2) Under prolonged hypoxia, tumor cell agent proliferation will also reduce.

Statistics and Reproducibility

Two-tailed Mann-Whitney U tests with a significance level of 0.05 were used for testing differences in simulated overall tumor progression (AUC) between conditions. Student's t-tests were used for comparing genetic effects metrics. P-value adjustment for multiple testing was performed using Benjamini-Hochberg correction. Boxplots show the median (center line), 25th–75th percentiles (box), and 1.5× IQR (whiskers). Points represent outliers.

Code Availability

The feature selection using LME model was performed in R (v4.2.2)[114]. ABM simulations were performed in Python (v3.9) [115] using the MESA framework (v2.2.4)[68]. The source code for reproducing the work is accessible at: https://github.com/KChen-lab/ABMACT.

Data Availability

Data for generating figures are provided in **Supplementary Data 4** and at https://doi.org/10.5281/zenodo.17818689. Public scRNA-seq data used in this work can be obtained from GSE190976, GSE227098, and syn52600685.

Acknowledgements

This work is made possible by 2024-345892 from the Chan Zuckerberg Initiative DAF, an advised fund of the Chan Zuckerberg Initiative Foundation, 5U01CA281902 from National Cancer Institute, and

75N99223S0001 from the Advanced Research Projects Agency for Health (ARPA-H). This work was supported in part by the University of Texas MD Anderson Cancer Center Institute for Cell Therapy Discovery & Innovation. The data used in this study were supported, in part, by grants (1 R01 CA211044-01, 5 P01CA148600-03, and U01CA247760) from the National Institutes of Health (NIH), the Cancer Prevention and Research Institute of Texas (grants RP180466 and RP180248), the Leukemia Specialized Program of Research Excellence (SPORE) Grant (P50CA100632), the Specialized Program of Research Excellence (SPORE) in Brain Cancer grant (P50CA127001), and CPRIT Single Core (RP180684), and a grant (P30 CA016672) from the NIH to the MD Anderson Cancer Center Flow Cytometry and Cellular Imaging Core Facility that assisted with the mass cytometry studies. We sincerely thank Drs. Peng Wei, Ziyi Li, Enli Liu, Li Li, and Ms. Xiaohan Chi for their support and insightful feedback during the development of the study.

Disclosure of conflicts of interests

The authors declare the following competing interests: M.Da., R.B., M.S., and K.R., and The University of Texas MD Anderson Cancer Center have an institutional financial conflict of interest with Takeda Pharmaceutical. R.B., K.R., and The University of Texas MD Anderson Cancer Center have an institutional financial conflict of interest with Affimed GmbH. K.R. participates on the Scientific Advisory Board for Avenge Bio, Virogin Biotech, Navan Technologies, Caribou Biosciences, Bit Bio Limited, Replay Holdings, oNKo Innate, and The Alliance for Cancer Gene Therapy ACGT. K.R. is the Scientific founder of Syena. M. Da. participates on the Scientific Advisory Board for Cellsbin.

Author contributions

Y.W. designed the study, developed all computational code, performed the analyses, and wrote the manuscript. S.C. contributed to study design, model development, interpretation of results, and manuscript writing. K.C. conceived and supervised the project, contributed to study design, model development, interpretation of results, and contributed to manuscript writing. M.Da., V.M., and E.D. generated and provided the experimental data, provided guidance throughout, and contributed to manuscript writing. M.S., L.L.P., R.B., and K.R. generated and provided the experimental data. M.De. contributed to project ideation and manuscript writing. All authors discussed the results and approved the final manuscript.

Table 1

Parameter	Description	Value	Unit	Source
p_C	Proliferation rate of cytotoxic NK cell	Vary by cell product	day^{-1}	Model fitting on data from Liu et al.[19]
d_C	Death rate of cytotoxic NK cell	Vary by cell product	day^{-1}	Model fitting on data from Liu et al.[19]
μ_c	Baseline NK cell cytotoxicity mean	Vary by cell product	Dimensionless	Model fitting on data from Li et al.[23]
σ_c	Baseline NK cell cytotoxicity standard deviation	0.01	Dimensionless	Fixed
b	NK cell cytotoxicity genetic effect coefficient	0.1	Dimensionless	Parameter search
γ	Chimeric antigen receptor effect exponent	CAR: 0.5 NT: 1.0	Dimensionless	Parameter search
$\beta_{G_{NK}}$	Coefficient vector of significant NK-cell cytotoxicity molecular features G	Supplementary Table S2	Dimensionless	LME model fitting on lymphoma mice model data in Li et al. [23]
g_{NK}	Normalized RNA expressions and GOBP densities of NK cells	Supplementary Data 1	Dimensionless	[23]
m_N	Movement probability of NK cells	0.9	Dimensionless	Fixed
v_N	Movement speed of NK cells	39	$\mu m \cdot hr^{-1}$	[116]
S_0	Initial NK cell serial killing capacity	Vary by cell product	cell	Model fitting on data from Marin et al.[5]
b_{p_c}	Natural decay parameter for cytotoxic NK cell proliferation rate	Vary by cell product	ΔT^{-1}	Model fitting on data from Liu et al.[19]

B_{50}	Half-maximum tumor load	25	Dimensionless	Model fitting on data from Liu et al.[19]
c_{50}	Half-maximum cytokine level	70	Dimensionless	Model fitting on data from Liu et al.[19]
γ_1	Hill's equation exponent of tumor antigen effect	0.2	Dimensionless	Model fitting on data from Liu et al.[19]
γ_2	Hill's equation exponent of cytokine effect	0.2	Dimensionless	Model fitting on data from Liu et al.[19]
$t_{50_{IL15}}$	Half-life of IL-15	2.5hr	ΔT^{-1}	[80]
$t_{50_{IL21}}$	Half-life of IL-21	0.2hr	ΔT^{-1}	[117]
$\mathrm{p}_{\mathrm{evade}}$	Probability of B cell lymphoma tumor cells evading immune surveillance	$\propto g^{-1}_{\{B,CD19\}}$	Dimensionless	[118]
p_V	Proliferation rate of vigilant NK cells	1e-3	day^{-1}	Fixed to be a small value based on literature [48,49,82–87]
d_V	Death rate of vigilant NK cells	1e-3	day^{-1}	Fixed to be a small value based on literature [48,49,82–87]
p_E	Proliferation rate of exhausted NK cells	0	day^{-1}	Fixed
d_E	Death rate of exhausted NK cells	Vary by cell product	day^{-1}	Model fitting on data from Liu et al.[19]
$k_{B\_}$	Transition probability of N_C to N_V	1.0	Dimensionless	Fixed
k_{B_+}	Transition probability of N_V to N_C	0.9	Dimensionless	Fixed
$p_{B_{lymphoma}}$	Proliferation rate of B cell lymphoma tumor cell	0.455	day^{-1}	Modeling fitting on data from Li et al.[56]

$p_{B_{glioblastoma}}$	Proliferation rate of glioblastoma tumor cell	0.223	day^{-1}	Modeling fitting on data from Shanley et al.[20]
d_B	Death rate of tumor cell	1e-4	day^{-1}	Modeling fitting on data from Li et al.[23]
m_B	Movement probability of tumor cells	0.1	Dimensionless	Fixed
v_B	Movement speed of tumor cells	1	$grid\ per\ step$	Fixed
p_{mutate}	Percentage increase of p_{evade}	1e-3	Dimensionless	Fixed
ΔT	Model step length	4	hr	[73]
l	Grid cell size	50	μm	Fixed
B_{Max}	Maximum number of tumor cells per grid cell	25	cell	Fixed

References

1. Li, H., Song, W., Li, Z. & Zhang, M. Preclinical and clinical studies of CAR-NK-cell therapies for malignancies. *Front Immunol* 13, (2022).
2. Laskowski, T. J., Biederstädt, A. & Rezvani, K. Natural killer cells in antitumour adoptive cell immunotherapy. *Nat Rev Cancer* 22, 557–575 (2022).
3. Boyiadzis, M. *et al.* Phase 1 clinical trial of adoptive immunotherapy using "off-the-shelf" activated natural killer cells in patients with refractory and relapsed acute myeloid leukemia. *Cytotherapy* 19, 1225–1232 (2017).
4. Williams, B. A. *et al.* A phase I trial of NK-92 cells for refractory hematological malignancies relapsing after autologous hematopoietic cell transplantation shows safety and evidence of efficacy. *Oncotarget* 8, 89256–89268 (2017).
5. Marin, D. *et al.* Safety, efficacy and determinants of response of allogeneic CD19-specific CAR-NK cells in CD19+ B cell tumors: a phase 1/2 trial. *Nature Medicine 2024 30:3* 30, 772–784 (2024).
6. Lee, D. W. *et al.* T cells expressing CD19 chimeric antigen receptors for acute lymphoblastic leukaemia in children and young adults: A phase 1 dose-escalation trial. *The Lancet* 385, 517–528 (2015).
7. Arai, S. *et al.* Infusion of the allogeneic cell line NK-92 in patients with advanced renal cell cancer or melanoma: A phase I trial. *Cytotherapy* 10, 625–632 (2008).
8. Geller, M. A. *et al.* A phase II study of allogeneic natural killer cell therapy to treat patients with recurrent ovarian and breast cancer. *Cytotherapy* 13, 98–107 (2011).
9. Rosenberg, S. A., Restifo, N. P., Yang, J. C., Morgan, R. A. & Dudley, M. E. Adoptive cell transfer: a clinical path to effective cancer immunotherapy. *Nat Rev Cancer* 8, 299–308 (2008).
10. Marofi, F. *et al.* CAR-engineered NK cells; a promising therapeutic option for treatment of hematological malignancies. *Stem Cell Res Ther* 12, (2021).
11. Rafei, H., Daher, M. & Rezvani, K. Chimeric antigen receptor (CAR) natural killer (NK)-cell therapy: leveraging the power of innate immunity. *Br J Haematol* 193, 216–230 (2021).
12. Rezvani, K., Rouce, R., Liu, E. & Shpall, E. Engineering Natural Killer Cells for Cancer Immunotherapy. *Molecular Therapy* 25, 1769–1781 (2017).
13. Daher, M., Melo Garcia, L., Li, Y. & Rezvani, K. CAR-NK cells: the next wave of cellular therapy for cancer. *Clin Transl Immunology* 10, (2021).
14. Lu, H., Zhao, X., Li, Z., Hu, Y. & Wang, H. From CAR-T Cells to CAR-NK Cells: A Developing Immunotherapy Method for Hematological Malignancies. *Front Oncol* 11, (2021).
15. Chu, J. *et al.* Natural killer cells: a promising immunotherapy for cancer. *J Transl Med* 20, 240 (2022).
16. Caruso, S. *et al.* Safe and effective off-the-shelf immunotherapy based on CAR.CD123-NK cells for the treatment of acute myeloid leukaemia. *J Hematol Oncol* 15, 163 (2022).
17. Romanski, A. *et al.* CD19-CAR engineered NK-92 cells are sufficient to overcome NK cell resistance in B-cell malignancies. *J Cell Mol Med* 20, 1287–1294 (2016).
18. Choi, E. *et al.* Engineering CD70-Directed CAR-NK Cells for the Treatment of Hematological and Solid Malignancies. *Blood* 138, 1691–1691 (2021).
19. Liu, E. *et al.* Cord blood NK cells engineered to express IL-15 and a CD19-targeted CAR show long-term persistence and potent anti-tumor activity. *Leukemia* 32, 520 (2018).
20. Shanley, M. *et al.* Interleukin-21 engineering enhances NK cell activity against glioblastoma via CEBPD. *Cancer Cell* 42, 1450-1466.e11 (2024).
21. Knelson, E. H. *et al.* Activation of Tumor-Cell STING Primes NK-Cell Therapy. *Cancer Immunol Res* 10, 947–961 (2022).
22. Daher, M. *et al.* Targeting a cytokine checkpoint enhances the fitness of armored cord blood CAR-NK cells. *Blood* 137, 624 (2021).
23. Li, L. *et al.* Loss of metabolic fitness drives tumor resistance after CAR-NK cell therapy and can be overcome by cytokine engineering. *Sci Adv* 9, eadd6997 (2023).

24. Kirouac, D. C., Zmurchok, C. & Morris, D. Making drugs from T cells: The quantitative pharmacology of engineered T cell therapeutics. *NPJ Syst Biol Appl* 10, 31 (2024).
25. Mak, I. W. Y., Evaniew, N. & Ghert, M. Lost in translation: animal models and clinical trials in cancer treatment. *Am J Transl Res* 6, 114 (2014).
26. Kaur, G. & Dufour, J. M. Cell lines: Valuable tools or useless artifacts. *Spermatogenesis* 2, 1–5 (2012).
27. Yang, S. *et al.* Organoids: The current status and biomedical applications. *MedComm (Beijing)* 4, (2023).
28. Metzcar, J., Wang, Y., Heiland, R. & Macklin, P. A Review of Cell-Based Computational Modeling in Cancer Biology. *JCO Clin Cancer Inform* 1–13 (2019) doi:10.1200/cci.18.00069.
29. del Sol, A. & Jung, S. The Importance of Computational Modeling in Stem Cell Research. *Trends Biotechnol* 39, 126–136 (2021).
30. Kirschner, D. E. & Linderman, J. J. Mathematical and computational approaches can complement experimental studies of host–pathogen interactions. *Cell Microbiol* 11, 531–539 (2009).
31. Walpole, J., Papin, J. A. & Peirce, S. M. Multiscale Computational Models of Complex Biological Systems. *Annu Rev Biomed Eng* 15, 137–154 (2013).
32. Chavali, A. K. *et al.* Characterizing emergent properties of immunological systems with multi-cellular rule-based computational modeling. *Trends Immunol* 29, 589–599 (2008).
33. Brodland, G. W. How computational models can help unlock biological systems. *Semin Cell Dev Biol* 47–48, 62–73 (2015).
34. Gilpin, L. H. *et al.* Explaining explanations: An overview of interpretability of machine learning. *Proceedings - 2018 IEEE 5th International Conference on Data Science and Advanced Analytics, DSAA 2018* 80–89 (2019) doi:10.1109/DSAA.2018.00018.
35. Feinberg, A. P. & Levchenko, A. Epigenetics as a mediator of plasticity in cancer. *Science (1979)* 379, (2023).
36. Gong, C. *et al.* A computational multiscale agent-based model for simulating spatio-temporal tumour immune response to PD1 and PDL1 inhibition. *J R Soc Interface* 14, (2017).
37. Bonabeau, E. Agent-based modeling: Methods and techniques for simulating human systems. *Proc Natl Acad Sci U S A* 99, 7280–7287 (2002).
38. Laubenbacher, R., Hinkelmann, F. & Oremland, M. Agent-Based Models and Optimal Control in Biology: A Discrete Approach. *Mathematical Concepts and Methods in Modern Biology: Using Modern Discrete Models* 143–178 (2013) doi:10.1016/B978-0-12-415780-4.00005-3.
39. Niida, A., Iwasaki, W. M., Niida, A. & Iwasaki, W. M. Agent-Based Modeling and Analysis of Cancer Evolution. *Simulation Modeling* https://doi.org/10.5772/INTECHOPEN.100140 (2021) doi:10.5772/INTECHOPEN.100140.
40. Kather, J. N. *et al.* In silico modeling of immunotherapy and stroma-targeting therapies in human colorectal cancer. *Cancer Res* 77, 6442–6452 (2017).
41. Retzlaff, J., Lai, X., Berking, C. & Vera, J. Integration of transcriptomics data into agent-based models of solid tumor metastasis. *Comput Struct Biotechnol J* 21, 1930 (2023).
42. Iwasaki, W. M. & Innan, H. Simulation framework for generating intratumor heterogeneity patterns in a cancer cell population. *PLoS One* 12, e0184229- (2017).
43. Kirouac, D. C. *et al.* Deconvolution of clinical variance in CAR-T cell pharmacology and response. *Nat Biotechnol* https://doi.org/10.1038/S41587-023-01687-X (2023) doi:10.1038/S41587-023-01687-X.
44. Kather, J. N. *et al.* In silico modeling of immunotherapy and stroma-targeting therapies in human colorectal cancer. *Cancer Res* 77, 6442–6452 (2017).
45. Rezvani, K. & Rouce, R. H. The Application of Natural Killer Cell Immunotherapy for the Treatment of Cancer. *Front Immunol* 6, (2015).
46. Pouxvielh, K. *et al.* Tumor-induced natural killer cell dysfunction is a rapid and reversible process uncoupled from the expression of immune checkpoints. *Sci Adv* 10, (2024).

47. Sun, J. C. & Lanier, L. L. NK cell development, homeostasis and function: parallels with CD8+ T cells. *Nat Rev Immunol* 11, 645–657 (2011).
48. Sun, J. C., Beilke, J. N., Bezman, N. A. & Lanier, L. L. Homeostatic proliferation generates long-lived natural killer cells that respond against viral infection. *J Exp Med* 208, 357 (2011).
49. Sun, J. C., Beilke, J. N. & Lanier, L. L. Adaptive immune features of natural killer cells. *Nature* 457, 557–561 (2009).
50. Kirouac, D. C. *et al.* Deconvolution of clinical variance in CAR-T cell pharmacology and response. *Nat Biotechnol* https://doi.org/10.1038/s41587-023-01687-x (2023) doi:10.1038/s41587-023-01687-x.
51. Gong, C. *et al.* A computational multiscale agent-based model for simulating spatio-temporal tumour immune response to PD1 and PDL1 inhibition. *J R Soc Interface* 14, (2017).
52. Dufva, O. *et al.* Single-cell functional genomics reveals determinants of sensitivity and resistance to natural killer cells in blood cancers. *Immunity* 56, 2816-2835.e13 (2023).
53. Du, X. *et al.* CD226 regulates natural killer cell antitumor responses via phosphorylation-mediated inactivation of transcription factor FOXO1. *Proc Natl Acad Sci U S A* 115, E11731–E11740 (2018).
54. Quatrini, L. *et al.* The Immune Checkpoint PD-1 in Natural Killer Cells: Expression, Function and Targeting in Tumour Immunotherapy. *Cancers (Basel)* 12, 1–21 (2020).
55. Tang, F. *et al.* A pan-cancer single-cell panorama of human natural killer cells. *Cell* 186, 4235-4251.e20 (2023).
56. Li, L. *et al.* Loss of metabolic fitness drives tumor resistance after CAR-NK cell therapy and can be overcome by cytokine engineering. *Sci Adv* 9, (2023).
57. Ran, G. he *et al.* Natural killer cell homing and trafficking in tissues and tumors: from biology to application. *Signal Transduct Target Ther* 7, 205 (2022).
58. Sanz-Ortega, L. *et al.* Redirecting NK cells to the lymph nodes to augment their lymphoma-targeting capacity. *NPJ Precis Oncol* 8, 1–12 (2024).
59. Yokoyama, W. M., Kim, S. & French, A. R. The Dynamic Life of Natural Killer Cells. *https://doi.org/10.1146/annurev.immunol.22.012703.104711* 22, 405–429 (2004).
60. Jamieson, A. M., Isnard, P., Dorfman, J. R., Coles, M. C. & Raulet, D. H. Turnover and Proliferation of NK Cells in Steady State and Lymphopenic Conditions. *The Journal of Immunology* 172, 864–870 (2004).
61. Rotte, A. *et al.* Dose–response correlation for CAR-T cells: a systematic review of clinical studies. *J Immunother Cancer* 10, e005678 (2022).
62. Frigault, M. *et al.* Dose fractionation of CAR-T cells. A systematic review of clinical outcomes. *Journal of Experimental & Clinical Cancer Research* 42, 11 (2023).
63. He, J. *et al.* Synergistic treatment strategy: combining CAR-NK cell therapy and radiotherapy to combat solid tumors. *Front Immunol* 14, (2023).
64. Mamo, T. *et al.* Infusion reactions in natural killer cell immunotherapy: a retrospective review. *Cytotherapy* 23, 627–634 (2021).
65. Hickey, J. W. *et al.* Integrating multiplexed imaging and multiscale modeling identifies tumor phenotype conversion as a critical component of therapeutic T cell efficacy. *Cell Syst* 15, 322-338.e5 (2024).
66. Dondossola, E. & La Posta, L. Natural Killer Cell Biology Study. *Division of Cancer Medicine, Department of Genitourinary Medical Oncology, The University of Texas MD Anderson Cancer Center, Houston, Texas* Preprint at (2025).
67. Cogno, N., Axenie, C., Bauer, R. & Vavourakis, V. Agent-based modeling in cancer biomedicine: applications and tools for calibration and validation. *Cancer Biol Ther* 25, (2024).
68. Kazil Jackie and Masad, D. and C. A. Utilizing Python for Agent-Based Modeling: The Mesa Framework. in *Social, Cultural, and Behavioral Modeling* (ed. Thomson Robert and Bisgin, H. and D. C. and H. A. and H. M.) 308–317 (Springer International Publishing, Cham, 2020).

69. Leonard-Duke, J. *et al.* Multiscale computational model predicts how environmental changes and drug treatments affect microvascular remodeling in fibrotic disease. https://doi.org/10.1101/2024.03.15.585249 (2024) doi:10.1101/2024.03.15.585249.
70. Kwon, T., Kwon, O.-S., Cha, H.-J. & Sung, B. J. Stochastic and Heterogeneous Cancer Cell Migration: Experiment and Theory. *Sci Rep* 9, 16297 (2019).
71. Herrera, L. *et al.* Adult peripheral blood and umbilical cord blood NK cells are good sources for effective CAR therapy against CD19 positive leukemic cells. *Scientific Reports 2019 9:1* 9, 1–10 (2019).
72. Han, J. J. FDA Modernization Act 2.0 allows for alternatives to animal testing. *Artif Organs* 47, 449–450 (2023).
73. Vanherberghen, B. *et al.* Classification of human natural killer cells based on migration behavior and cytotoxic response. *Blood* 121, 1326–1334 (2013).
74. Castriconi, R. *et al.* Molecular Mechanisms Directing Migration and Retention of Natural Killer Cells in Human Tissues. *Front Immunol* 9, 2324 (2018).
75. Topham, N. J. & Hewitt, E. W. Natural killer cell cytotoxicity: how do they pull the trigger? *Immunology* 128, 7 (2009).
76. Paul, S. & Lal, G. The molecular mechanism of natural killer cells function and its importance in cancer immunotherapy. *Front Immunol* 8, 290728 (2017).
77. Virtanen, P. *et al.* SciPy 1.0: fundamental algorithms for scientific computing in Python. *Nat Methods* 17, 261–272 (2020).
78. Hermans, L. & O'Sullivan, T. E. No time to die: Epigenetic regulation of natural killer cell survival. *Immunological Reviews* Preprint at https://doi.org/10.1111/imr.13314 (2024).
79. Padmanabhan, R. & Meskin, N. Mathematical Modeling on Immunotherapy and Its Application for Deriving Cancer Therapy. in *Handbook of Cancer and Immunology* 1–33 (Springer International Publishing, Cham, 2022). doi:10.1007/978-3-030-80962-1_314-1.
80. Hangasky, J. A. *et al.* A very long-acting IL-15: implications for the immunotherapy of cancer. *J Immunother Cancer* 10, e004104 (2022).
81. Bhat, R. & Watzl, C. Serial killing of tumor cells by human natural killer cells - Enhancement by therapeutic antibodies. *PLoS One* 2, (2007).
82. Sun, J. C. & Lanier, L. L. NK cell development, homeostasis and function: Parallels with CD8 + T cells. *Nat Rev Immunol* 11, 645–657 (2011).
83. Stary, V. & Stary, G. NK Cell-Mediated Recall Responses: Memory-Like, Adaptive, or Antigen-Specific? *Front Cell Infect Microbiol* 10, (2020).
84. Gang, M. *et al.* CAR-modified memory-like NK cells exhibit potent responses to NK-resistant lymphomas. *Blood* 136, 2308 (2020).
85. Paust, S., Blish, C. A. & Reeves, R. K. Redefining Memory: Building the Case for Adaptive NK Cells. *J Virol* 91, (2017).
86. Guo, C. *et al.* Single-cell transcriptomics reveal a unique memory-like NK cell subset that accumulates with ageing and correlates with disease severity in COVID-19. *Genome Med* 14, (2022).
87. Sun, J. C., Beilke, J. N. & Lanier, L. L. Adaptive immune features of natural killer cells. *Nature 2009 457:7229* 457, 557–561 (2009).
88. Sherr, C. J. Cancer Cell Cycles. *Science (1979)* 274, 1672–1677 (1996).
89. Ali, A. E. *et al.* Classifying B-cell non-Hodgkin lymphoma by using MIB-1 proliferative index in fine-needle aspirates. *Cancer Cytopathol* 118, 166–172 (2010).
90. Feucht, D. *et al.* Preoperative growth dynamics of untreated glioblastoma: Description of an exponential growth type, correlating factors, and association with postoperative survival. *Neurooncol Adv* 6, (2024).
91. Duesberg, P., Stindl, R. & Hehlmann, R. Explaining the high mutation rates of cancer cells to drug and multidrug resistance by chromosome reassortments that are catalyzed by aneuploidy. *Proc Natl Acad Sci U S A* 97, 14295–300 (2000).

92. Liang, Q., Huang, Y., He, S. & Chen, K. Pathway centric analysis for single-cell RNA-seq and spatial transcriptomics data with GSDensity. *Nature Communications 2023 14:1* 14, 1–17 (2023).
93. Long, E. O., Sik Kim, H., Liu, D., Peterson, M. E. & Rajagopalan, S. Controlling NK Cell Responses: Integration of Signals for Activation and Inhibition. *Annu Rev Immunol* 31, 227–258 (2013).
94. Jia, H., Yang, H., Xiong, H. & Luo, K. Q. NK cell exhaustion in the tumor microenvironment. *Front Immunol* 14, (2023).
95. Littwitz-Salomon, E. *et al.* Metabolic requirements of NK cells during the acute response against retroviral infection. *Nat Commun* 12, 5376 (2021).
96. Wang, F. *et al.* TIGIT expression levels on human NK cells correlate with functional heterogeneity among healthy individuals. *Eur J Immunol* 45, 2886–2897 (2015).
97. Wennerberg, E., Kremer, V., Childs, R. & Lundqvist, A. CXCL10-induced migration of adoptively transferred human natural killer cells toward solid tumors causes regression of tumor growth in vivo. *Cancer Immunology, Immunotherapy* 64, 225–235 (2015).
98. Bates, D., Mächler, M., Bolker, B. & Walker, S. Fitting Linear Mixed-Effects Models Using lme4. *J Stat Softw* 67, (2015).
99. Liu, D.-H., Mou, F.-F., An, M. & Xia, P. Human leukocyte antigen and tumor immunotherapy (Review). *Int J Oncol* 62, 68 (2023).
100. Savoia, P., Fava, P., Casoni, F. & Cremona, O. Targeting the ERK Signaling Pathway in Melanoma. *Int J Mol Sci* 20, 1483 (2019).
101. Novikov, N. M., Zolotaryova, S. Y., Gautreau, A. M. & Denisov, E. V. Mutational drivers of cancer cell migration and invasion. *Br J Cancer* 124, 102–114 (2021).
102. Cannon, A. C., Uribe-Alvarez, C. & Chernoff, J. RAC1 as a Therapeutic Target in Malignant Melanoma. *Trends Cancer* 6, 478–488 (2020).
103. Zheng, F. *et al.* The HIF-1α antisense long non-coding RNA drives a positive feedback loop of HIF-1α mediated transactivation and glycolysis. *Nat Commun* 12, 1341 (2021).
104. Yang, Y. & Cao, Y. The impact of VEGF on cancer metastasis and systemic disease. *Semin Cancer Biol* 86, 251–261 (2022).
105. Pedregosa, F. *et al.* Scikit-learn: Machine Learning in Python. *Journal of Machine Learning Research* 12, 2825–2830 (2011).
106. Korotkevich, G. *et al.* Fast gene set enrichment analysis. *bioRxiv* 060012 (2021) doi:10.1101/060012.
107. Scornet, E. Trees, forests, and impurity-based variable importance in regression. *Annales de l'Institut Henri Poincaré, Probabilités et Statistiques* https://api.semanticscholar.org/CorpusID:210164587 (2020).
108. Altmann, A., Toloşi, L., Sander, O. & Lengauer, T. Permutation importance: a corrected feature importance measure. *Bioinformatics* 26, 1340–1347 (2010).
109. Nikishova, A., Veen, L., Zun, P. & Hoekstra, A. G. Uncertainty Quantification of a Multiscale Model for In-Stent Restenosis. *Cardiovasc Eng Technol* 9, 761–774 (2018).
110. Boelts, J. *et al.* sbi reloaded: a toolkit for simulation-based inference workflows. *J Open Source Softw* 10, 7754 (2025).
111. Papamakarios, G. & Murray, I. Fast $ε$-free Inference of Simulation Models with Bayesian Conditional Density Estimation. (2018).
112. Jalalimanesh, A., Shahabi Haghighi, H., Ahmadi, A. & Soltani, M. Simulation-based optimization of radiotherapy: Agent-based modeling and reinforcement learning. *Math Comput Simul* 133, 235–248 (2017).
113. McKeown, S. R. Defining normoxia, physoxia and hypoxia in tumours—implications for treatment response. *Br J Radiol* 87, 20130676 (2014).
114. Team, R. C. R: A Language and Environment for Statistical Computing. Preprint at https://www.R-project.org/ (2022).

115. Foundation, P. S. Python 3.9: A Programming Language. Preprint at https://www.python.org/ (2020).
116. Olofsson, P. E. *et al.* Distinct migration and contact dynamics of resting and IL-2-activated human natural killer cells. *Front Immunol* 5, (2014).
117. Bhatt, S. *et al.* Anti-CD20-interleukin-21 fusokine targets malignant B cells via direct apoptosis and NK-cell–dependent cytotoxicity. *Blood* 129, 2246–2256 (2017).
118. Wang, K., Wei, G. & Liu, D. CD19: a biomarker for B cell development, lymphoma diagnosis and therapy. *Exp Hematol Oncol* 1, 36 (2012).

Editor Summary

ABMACT, an agent-based model of adoptive cell therapy, recapitulated cellular dynamics in two cancer preclinical models and showed that enhancing immune cell proliferation, cytotoxicity, and serial killing capacity is critical for optimal efficacy.

Peer review information
Communications Biology thanks Christopher Schorr, Sadegh Marzban and the other, anonymous, reviewer(s) for their contribution to the peer review of this work. Primary Handling Editors: Dr. Nilanjan Banerjee and Dr. Laura Rodriguez Perez.

Agent-Based Model for Adoptive Cell Therapy

1 Cell Agent Design

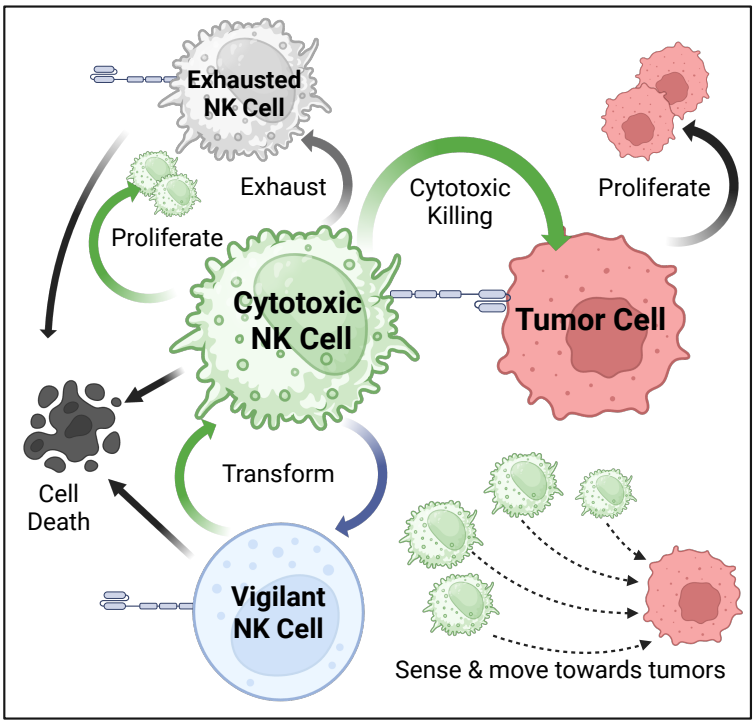

2 Integrate Functional Genetic Effects

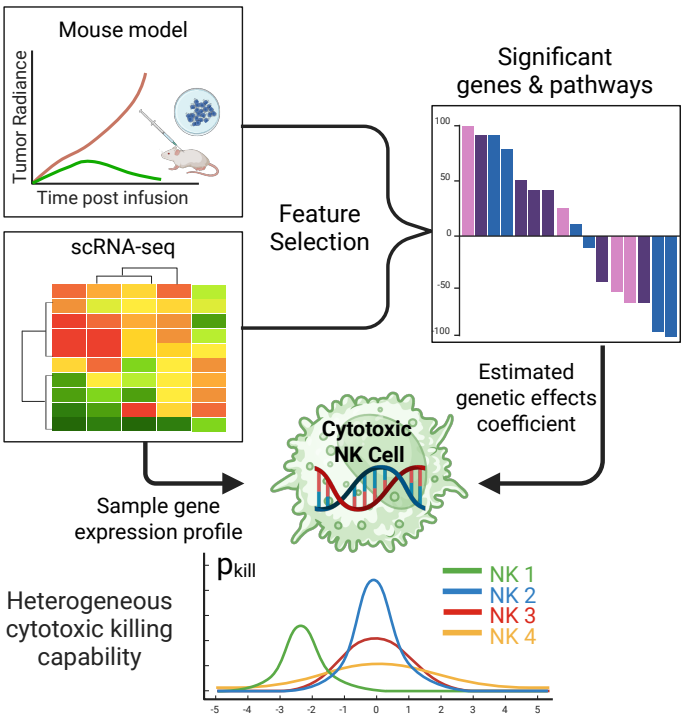

3 Model Calibration

In Vitro and In Vivo Experiment Data

- NK cell autonomous growth
- Dose-response assay
- Co-culture rechallenge assay
- PDX mouse model

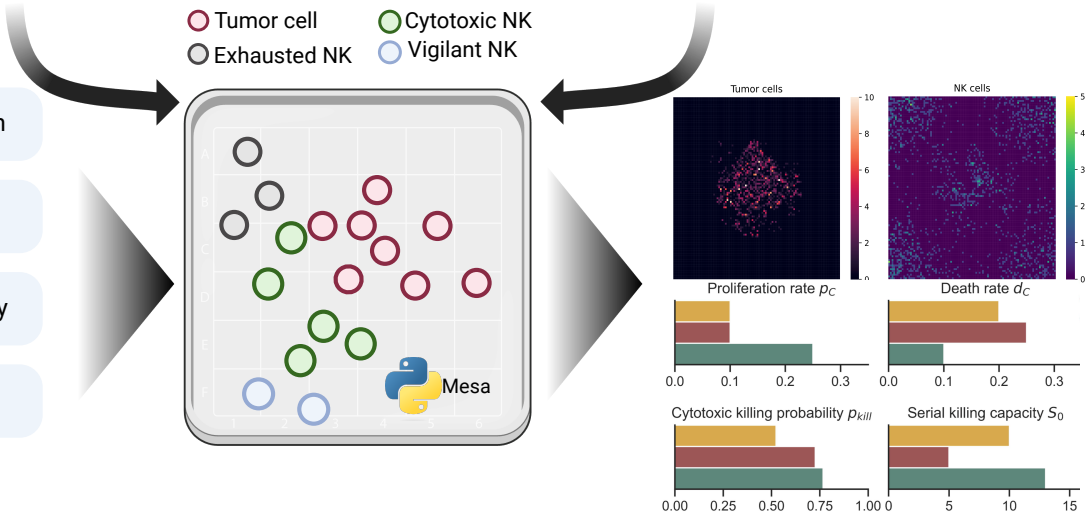

4 Applications

Augment Data & Predict

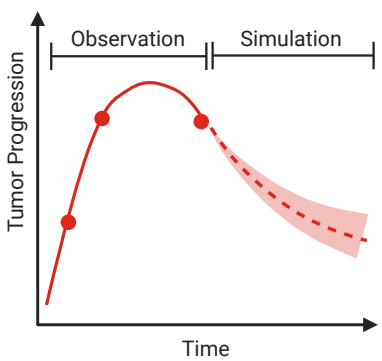

Efficacy Driver Discovery

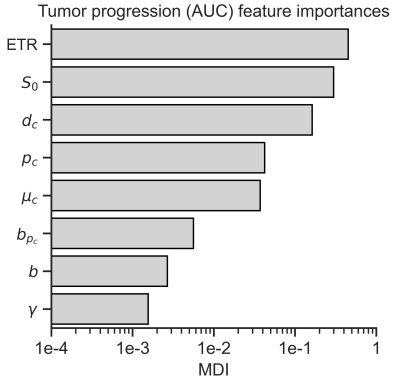

In Silico Treatment Simulation

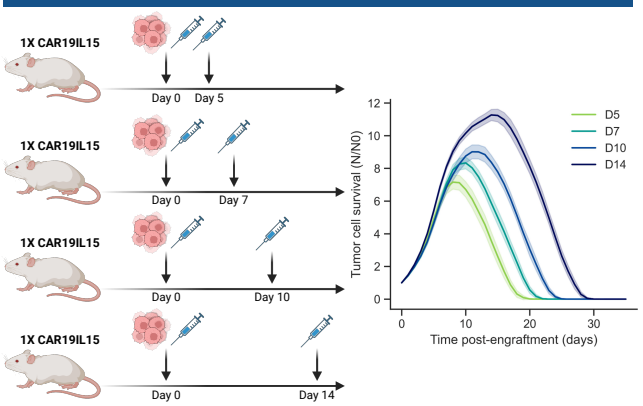

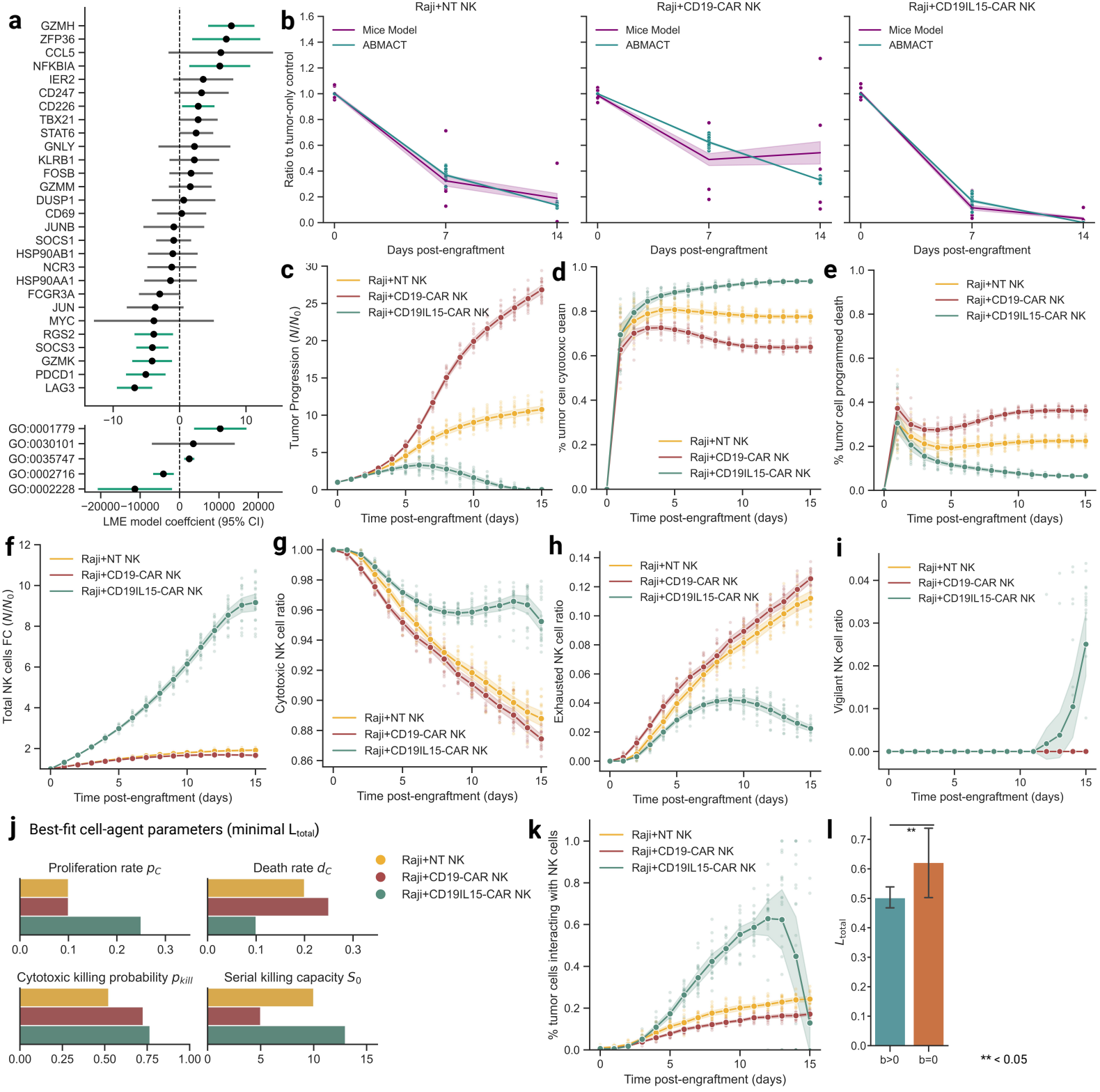
a
GZMH
ZFP36
CCL5
NFKBIA
IER2
CD247
CD226
TBX21
STAT6
GNLY
KLRB1
FOSB
GZMM
DUSP1
CD69
JUNB
SOCS1
HSP90AB1
NCR3
HSP90AA1
FCGR3A
JUN
MYC
RGS2
SOCS3
GZMK
PDCD1
LAG3
GO:0001779
GO:0030101
GO:0035747
GO:0002716
GO:0002228
LME model coeffcient (95% CI)
b
Raji+NT NK
Raji+CD19-CAR NK
Raji+CD19IL15-CAR NK
Mice Model
ABMACT
Ratio to tumor-only control
Days post-engraftment
c
Tumor Progression (N/N0)
Time post-engraftment (days)
d
% tumor cell cytotoxic death
e
% tumor cell programmed death
f
Total NK cells FC (N/N0)
g
Cytotoxic NK cell ratio
h
Exhausted NK cell ratio
i
Vigilant NK cell ratio
j
Best-fit cell-agent parameters (minimal Ltotal)
Proliferation rate pC
Death rate dC
Cytotoxic killing probability pkill
Serial killing capacity S0
k
% tumor cells interacting with NK cells
l
Ltotal
b>0
b=0
** < 0.05

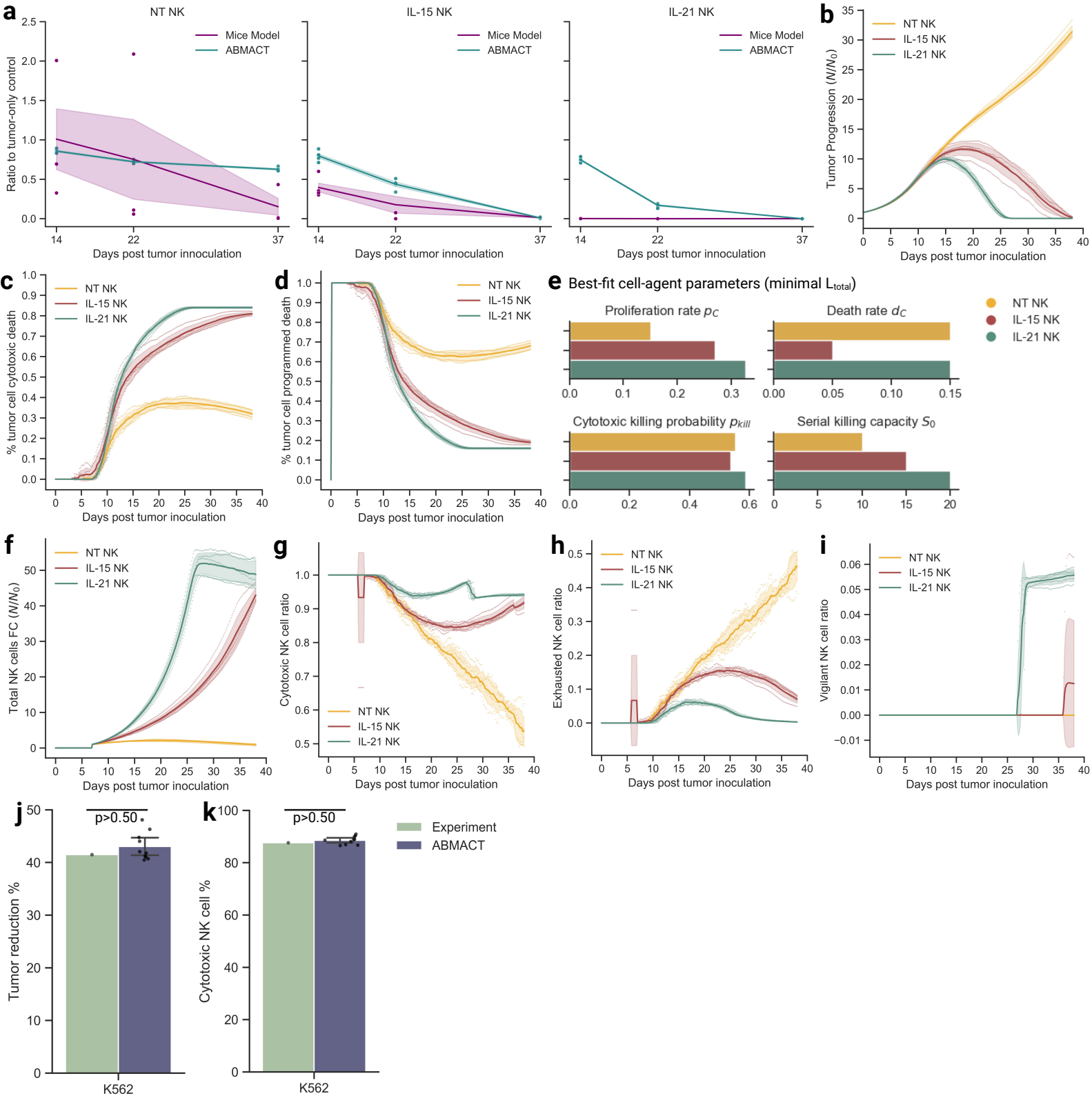
a
NT NK
IL-15 NK
IL-21 NK
Mice Model
ABMACT
Ratio to tumor-only control
Days post tumor innoculation
b
NT NK
IL-15 NK
IL-21 NK
Tumor Progression (N/N0)
Days post tumor inoculation
c
% tumor cell cytotoxic death
Days post tumor inoculation
d
% tumor cell programmed death
Days post tumor inoculation
e
Best-fit cell-agent parameters (minimal Ltotal)
Proliferation rate pC
Death rate dC
Cytotoxic killing probability pkill
Serial killing capacity S0
f
Total NK cells FC (N/N0)
Days post tumor inoculation
g
Cytotoxic NK cell ratio
Days post tumor inoculation
h
Exhausted NK cell ratio
Days post tumor inoculation
i
Vigilant NK cell ratio
Days post tumor inoculation
j
p>0.50
Tumor reduction %
K562
k
p>0.50
Experiment
ABMACT
Cytotoxic NK cell %
K562

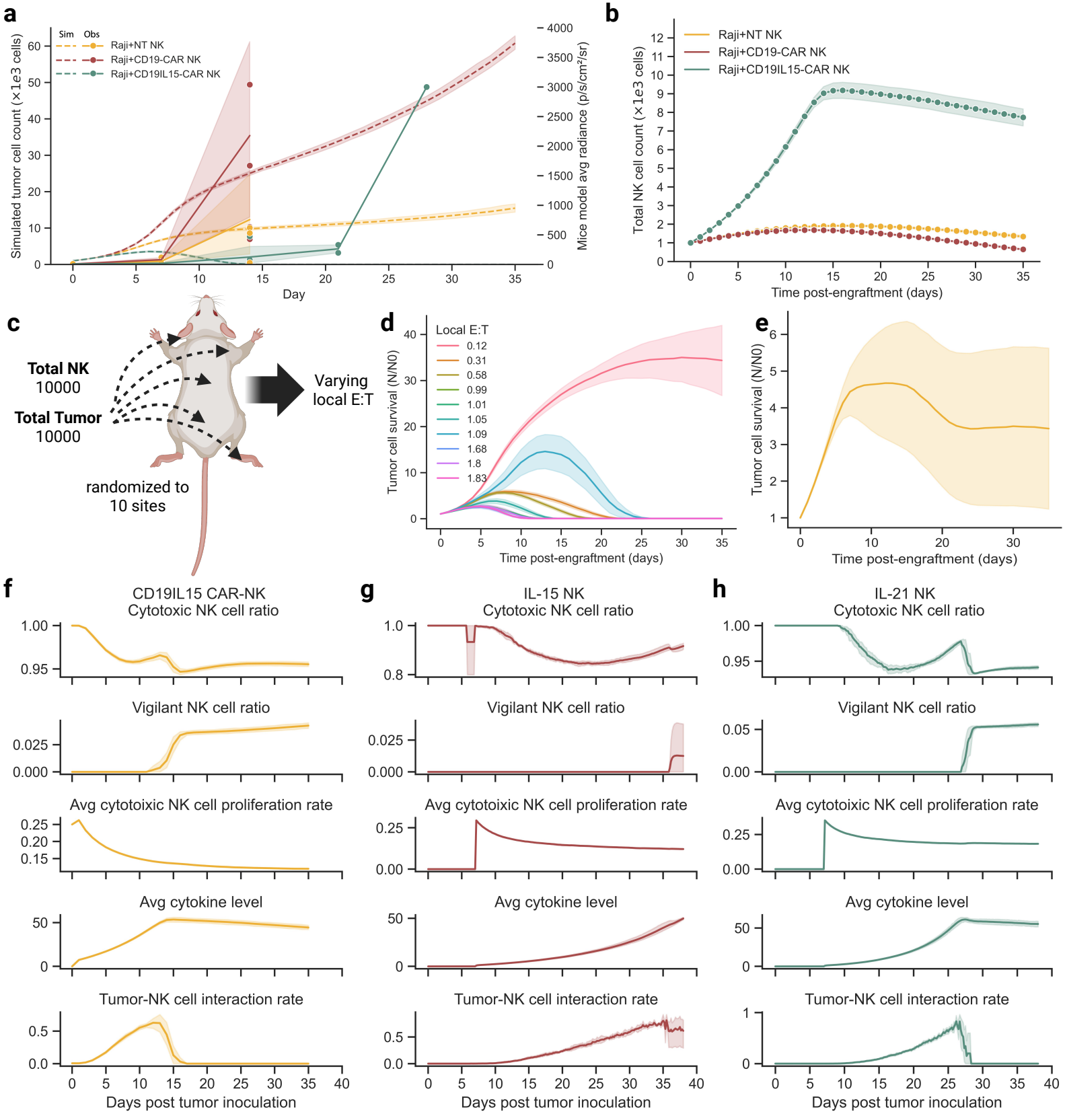
a
Sim Obs
Raji+NT NK
Raji+CD19-CAR NK
Raji+CD19IL15-CAR NK
Simulated tumor cell count (×1e3 cells)
Mice model avg radiance (p/s/cm²/sr)
Day
b
Raji+NT NK
Raji+CD19-CAR NK
Raji+CD19IL15-CAR NK
Total NK cell count (×1e3 cells)
Time post-engraftment (days)
c
Total NK
10000
Total Tumor
10000
randomized to
10 sites
Varying
local E:T
d
Local E:T
0.12
0.31
0.58
0.99
1.01
1.05
1.09
1.68
1.8
1.83
Tumor cell survival (N/N0)
Time post-engraftment (days)
e
Tumor cell survival (N/N0)
Time post-engraftment (days)
f
CD19IL15 CAR-NK
Cytotoxic NK cell ratio
Vigilant NK cell ratio
Avg cytotoixic NK cell proliferation rate
Avg cytokine level
Tumor-NK cell interaction rate
Days post tumor inoculation
g
IL-15 NK
Cytotoxic NK cell ratio
Vigilant NK cell ratio
Avg cytotoixic NK cell proliferation rate
Avg cytokine level
Tumor-NK cell interaction rate
Days post tumor inoculation
h
IL-21 NK
Cytotoxic NK cell ratio
Vigilant NK cell ratio
Avg cytotoixic NK cell proliferation rate
Avg cytokine level
Tumor-NK cell interaction rate
Days post tumor inoculation

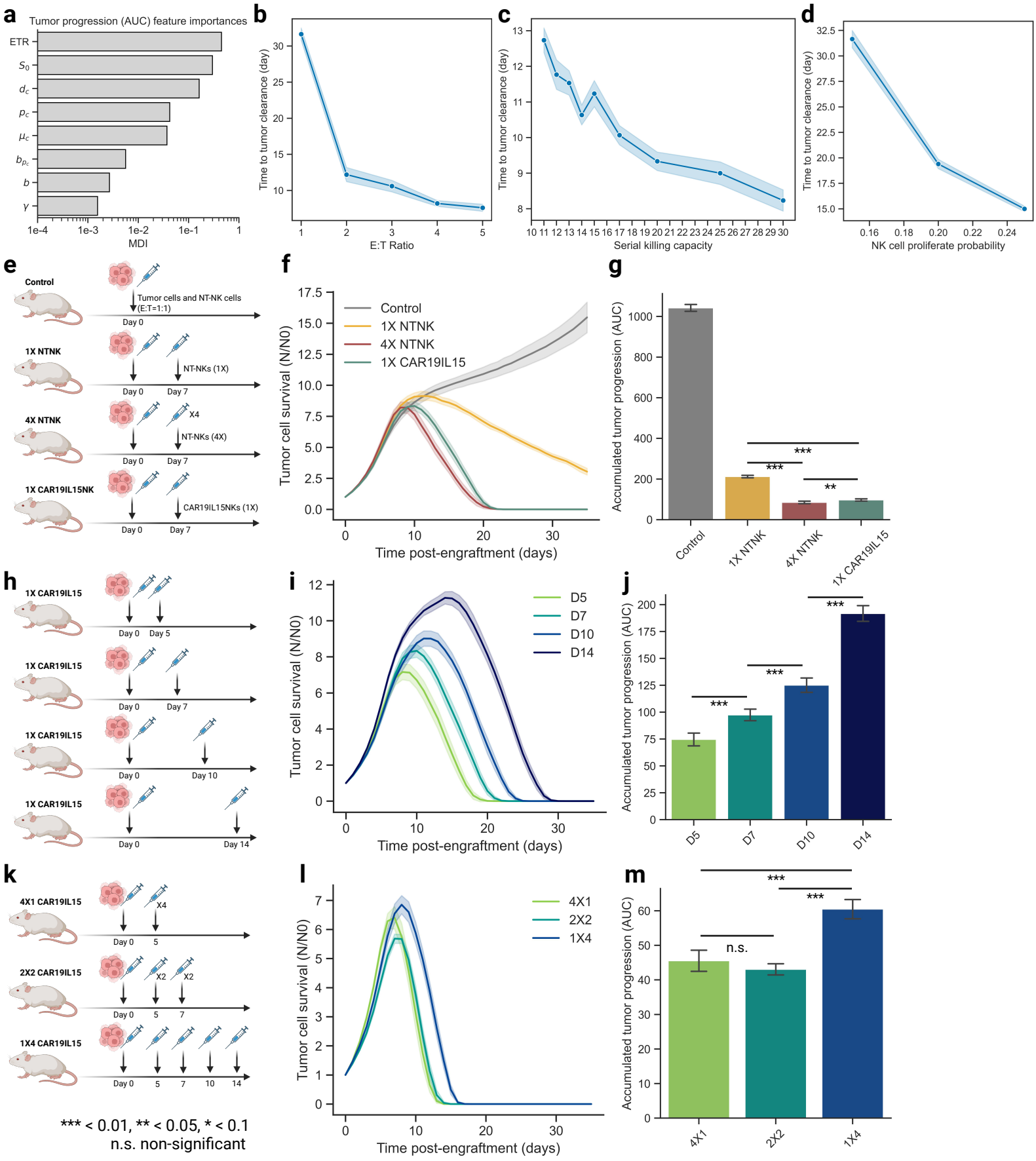

*** < 0.01, ** < 0.05, * < 0.1
n.s. non-significant